JOURNAL OF GEOPHYSICAL RESEARCH, VOL. 112, D10310, doi:10.1029/2006JD007953, 2007

The impact of interannual variability on multidecadal total ozone simulations

Eric L. Fleming,[1,2] Charles H. Jackman,[1] Debra K. Weisenstein,[3] and Malcolm K. W. Ko[4]

Received 23 August 2006; revised 14 December 2006; accepted 23 January 2007; published 23 May 2007.

[1] We have used a two-dimensional chemistry and transport model to study the effects of interannual dynamical variability on global total ozone for 1979–2004. Long-term meteorological data from the National Centers for Environmental Prediction-National Center for Atmospheric Research (NCEP-NCAR) reanalysis-2 project and the European Center for Medium Range Weather Forecasts (ECMWF) updated reanalysis (ERA-40) are used to construct yearly dynamical fields for use in the model. The simulations qualitatively resolve much of the seasonal and interannual variability observed in long-term global total ozone data, including fluctuations related to the quasi-biennial oscillation (QBO). We performed a series of model experiments to examine the relative roles of the interannual variability, changes in halogen and volcanic aerosol loading, and the 11-year solar cycle in controlling the multidecadal ozone changes. Statistical regression is used to isolate these signals in the observed and simulated time series. At Northern midlatitudes, the simulated interannual dynamical variability acts to reinforce the chemical ozone depletion caused by the enhanced aerosol loading following the eruption of Mt. Pinatubo in 1991. However, at Southern midlatitudes, the interannual variability masks the aerosol-induced chemical effect. The simulated solar cycle response in total ozone is generally consistent with observations and is primarily due to the direct photochemical effect. The halogen-induced total ozone trend for 1979–1996 derived from the model is in good agreement with that derived from observations in the tropics and the Northern Hemisphere (NH). However, at Southern midlatitudes, the trend derived from the model is more sensitive to halogen loading than that derived from observations.

Citation: Fleming, E. L., C. H. Jackman, D. K. Weisenstein, and M. K. W. Ko (2007), The impact of interannual variability on multidecadal total ozone simulations, *J. Geophys. Res.*, *112*, D10310, doi:10.1029/2006JD007953.

1. Introduction

[2] Stratospheric ozone underwent significant decreases during the 1980s and 1990s, and much of the ozone depletion was attributed to man-made factors [e.g., *World Meteorological Organization (WMO)*, 1999, 2003, 2007]. Natural variations that impact ozone on long-term multiyear timescales include stratospheric sulfate aerosol loading caused by major volcanic eruptions and the 11-year solar cycle variation in ultraviolet (UV) flux. Earlier studies using two-dimensional models investigated the relative roles of these processes in controlling long-term ozone changes [e.g., *Solomon et al.*, 1996, 1998; *Jackman et al.*, 1996; *Geller and Smyshlyaev*, 2002].

[3] The impact on ozone of year-to-year and longer term changes in transport and temperature has also received increased scrutiny in recent years, especially with the development of long-term meteorological data sets. Two particular dynamical effects are thought to influence ozone at middle and high latitudes: (1) changes in the strength of the Brewer-Dobson circulation, which is driven by stratospheric planetary wave drag, and the resulting transport of ozone from the tropical source region into the extratropics [e.g., *Fusco and Salby*, 1999; *Randel et al.*, 2002; *Salby and Callaghan*, 2004b; *Hood and Soukharev*, 2003, 2005]; and (2) changes in the tropospheric circulation, including changes in synoptic wave events and the tropopause height [e.g., *Steinbrecht et al.*, 1998, 2001; *Hood et al.*, 1997, 2001; *Reid et al.*, 2000; *Orsolini and Limpasuvan*, 2001].

[4] Previous two-dimensional model studies have utilized meteorological data to incorporate interannual changes in the residual circulation in the model simulations. These investigations were able to capture some of the yearly changes, including those related to the quasi-biennial oscillation (QBO), seen in observations of total ozone and long-lived tracers in the tropics [e.g., *Callis et al.*, 1997; *Fleming et al.*, 2002; *Jiang et al.*, 2004]. Also, the two-dimensional model study of *Jackman et al.* [1991] resolved a good deal of the interannual variability in upper stratospheric ozone at low to middle latitudes, where temperature-dependent

[1]NASA Goddard Space Flight Center, Greenbelt, Maryland, USA.
[2]Also at Science Systems and Applications, Inc., Lanham, Maryland, USA.
[3]Atmospheric and Environmental Research, Inc., Lexington, Massachusetts, USA.
[4]NASA Langley Research Center, Hampton, Virginia, USA.

0148-0227/07/2006JD007953$09.00

photochemistry controls the ozone distribution. Other studies have utilized interactive two-dimensional models to investigate the processes that generate interannual and QBO-like variations in ozone and tracers in the tropics and extratropics [e.g., *Gray and Ruth*, 1993; *Kinnersley and Tung*, 1998, 1999; *Jones et al.*, 1998]. More recently, studies have investigated the role of interannual transport variations on ozone utilizing three-dimensional chemical transport models (CTMs) driven by winds and temperatures from (1) meteorological analyses [e.g., *Hadjinicolaou et al.*, 1997, 2002, 2005; *Chipperfield*, 1999, 2003; *Chipperfield and Jones*, 1999] and (2) a general circulation model [e.g., *Stolarski et al.*, 2006].

[5] Although more and more work is being done utilizing three-dimensional CTMs given the computational power now available, two-dimensional models remain useful for stratospheric ozone studies. Their flexibility and speed (15 min clock time per model year) allow numerous sensitivity simulations to be performed in a small amount of time. Furthermore, as discussed previously and summarized in this study, the zonal mean residual circulation framework provides a good representation of stratospheric transport processes and good simulations of tracers in the meridional plane.

[6] Our two-dimensional chemistry and transport model at NASA/Goddard Space Flight Center (GSFC) has been widely used in scientific and assessment studies of the long-term changes in stratospheric ozone [e.g., *Jackman et al.*, 1996; *WMO*, 1999, 2003, 2007]. More recently, we have investigated interannual variability in the tropical stratosphere for the 1990s, utilizing global meteorological analyses to derive yearly model transport fields [*Fleming et al.*, 2002]. Since that study, our model has undergone significant changes in the treatment of chemistry and transport processes.

[7] In the present paper, we describe our updated model and build on previous work to study the interannual variations in total column ozone on a global basis for the 1979–2004 time period. Here we utilize winds and temperatures from two meteorological data sets to derive the zonal mean model transport parameters. Previous empirical studies have illustrated the influence of yearly changes in the planetary-wave-driven residual circulation in controlling the interannual anomalies in extratropical temperature and total ozone [e.g., *Fusco and Salby*, 1999; *Newman et al.*, 2001; *Randel et al.*, 2002]. In this study, we will specifically examine how much of the seasonal and interannual variability observed in long-term satellite-based total ozone data can be explained using this two-dimensional model methodology. We will then examine the relative roles that halogen and aerosol loading, solar cycle changes, and interannual dynamical variability have on the long-term modeled ozone simulations. We will also investigate how interannual variability affects the modeled responses to the solar cycle and volcanic aerosol-induced ozone changes, as well as the long-term total ozone trends.

2. GSFC Two-Dimensional Model

[8] The latest version of our GSFC two-dimensional model was used in this study. This model was originally discussed in the works of *Douglass et al.* [1989] and *Jackman et al.* [1990] and has undergone extensive upgrades over the years [e.g., *Considine et al.*, 1994; *Jackman et al.*, 1996; *Fleming et al.*, 1999; *Jackman et al.*, 2005]. In this section, we summarize our latest model improvements.

2.1. Model Transport

[9] In a previous investigation [*Fleming et al.*, 2002], we derived two-dimensional model transport fields from winds and temperatures of the United Kingdom Meteorological Office (UKMO) data assimilation system to study yearly constituent changes in the tropical stratosphere for 1992–2000. In a similar fashion, we now use meteorological analyses to compile yearly radiative heating rates and zonal mean and eddy flux quantities for the time period 1958–2004. These fields are then used to derive our two-dimensional model residual meridional circulation and horizontal and vertical eddy diffusion quantities as discussed in the study of *Fleming et al.* [1999, 2002] and summarized below. Previous studies have shown that meteorological analyses tend to underestimate the QBO temperature amplitude in the equatorial stratosphere [*Randel et al.*, 1999; *Huesmann and Hitchman*, 2001]. To obtain a more realistic meridional QBO circulation in our model, we follow the parameterizations of *Dunkerton* [1997] to account for the eddy momentum forcing from large-scale, long-period Kelvin and Rossby-Gravity waves and a continuous spectrum of gravity waves in the tropical stratosphere.

[10] We will show model results primarily using data from the National Centers for Environmental Prediction-National Center for Atmospheric Research (NCEP-NCAR) reanalysis-2 project [*Kalnay et al.*, 1996; *Kistler et al.*, 2001; *Kanamitsu et al.*, 2002]. These data cover the time period 1958–present and extend from the surface to 10 mbar. For the upper stratosphere (10–1 mbar), we use the original NCEP analyses data [*Gelman et al.*, 1986], which cover the time period 1979–present. Prior to 1979, we use climatologically averaged fields for the region above 10 mbar. To evaluate the robustness of the simulated interannual variations, we will also show results utilizing the European Center for Medium Range Weather Forecasts (ECMWF) updated reanalysis (ERA-40) data [*Uppala et al.*, 2005: see also the Web site: http://www.ECMWF.int]. The ERA-40 extend from the surface to 1 mbar for the period September 1957–August 2002.

[11] For the mesosphere for 1–0.002 mbar (~50–90 km), we employ the temperature measurements made by the Microwave Limb Sounder (MLS) onboard the Upper Atmosphere Research Satellite (UARS) for September 1991 through June 1997 [*Wu et al.*, 2003]. Here we use the MLS temperatures along with the 1-mbar UKMO geopotential heights to derive u- and v-component balanced winds and the resulting eddy heat and momentum fluxes [e.g., *Randel*, 1987]. The MLS temperatures are also used to compute zonal mean diabatic heating rates for the mesosphere. For all model simulations, we use the yearly varying MLS-derived quantities for 1991–1997. Prior to September 1991 and post June 1997, a yearly repeating climatological average of the MLS data is used for the model simulations.

[12] The heating rate calculations for this work are based on *Rosenfield et al.* [1994, 1997], with updates to the parameterization for the solar absorption due to water vapor in the infrared [*Chou and Suarez*, 1999], the thermal infrared parameterization [*Chou et al.*, 2001], and the

International Satellite Cloud Climatology Project cloud climatology [*Rossow and Duenas*, 2004]. We have also included the effects of the solar cycle UV variation in the solar heating rate calculation. The yearly variations of ozone and water vapor used in the heating rates are not coupled to the model chemistry. Rather, we use a combination of Solar Backscattered Ultraviolet Radiometer (SBUV), Stratospheric Aerosol and Gas Experiment II (SAGE II), and UARS data for 1979–2004 where available. Values prior to 1979 are set to a monthly mean climatological average of these data.

[13] The vertical eddy diffusion rates (K_{zz}) in the upper stratosphere and mesosphere are based on the gravity wave parameterization originally developed by *Lindzen* [1981] and modified by *Holton and Zhu* [1984]. For the troposphere and lower stratosphere, K_{zz} is based on the zonal mean temperature lapse rate. We specify a lower limit of 0.01 m^2/s in the equatorial lower stratosphere to be consistent with previous observational analyses of tracer data [*Hall and Waugh*, 1997; *Mote et al.*, 1998]. For the current work, we have modestly increased the upper troposphere/lower stratospheric K_{zz} at middle and high latitudes compared with what we have used previously. This faster stratosphere-troposphere exchange rate gives improved model comparisons with a variety of long-lived tracer data.

[14] The horizontal eddy diffusion (K_{yy}) is derived consistently with the circulation as the ratio of the Eliassen-Palm (E-P) flux divergence to the latitudinal gradient of zonal mean potential vorticity ($\bar{q}_y$) [*Newman et al.*, 1988; *Randel and Garcia*, 1994]. We have also incorporated a new off-diagonal eddy diffusion calculation (K_{yz}) in the model, which is adapted from the Atmospheric Environmental Research, Inc. (AER) two-dimensional model [*Schneider et al.*, 1989]. This follows the assumption that horizontal eddy mixing is directed along the zonal mean isentropes and projects the K_{yy} mixing rates onto isentropic surfaces [*Plumb and Mahlman*, 1987; *Newman et al.*, 1988].

[15] The residual circulation ($\bar{v}^*$, $\bar{w}^*$) is derived from the input heating rates, eddy fluxes, zonal mean temperature and zonal wind fields following the methodology originally outlined by *Garcia and Solomon* [1983]. The diffusion and residual circulation fields are computed from 31-day running averages of the input quantities. This is necessitated by the need for monthly averaged K_{yy} values for two-dimensional model transport as the concept for deriving K_{yy} is problematic for shorter timescales [*Plumb and Mahlman*, 1987; *Newman et al.*, 1988]. Uncertainties in these zonal mean transport fields arise from the assumptions used in the formulations and from uncertainties in the input data sets (i.e., meteorological fields, ozone, and water vapor data used in the heating rates). Discussion of these uncertainties can be found in previous work [e.g., *Garcia and Solomon*, 1983; *Plumb and Mahlman*, 1987; *Andrews et al.*, 1987; *Newman et al.*, 1988; *Fleming et al.*, 2001].

2.2. Model Chemistry

[16] The model chemistry domain extends from the ground to approximately 92 km, with a variable grid resolution that is determined by the user. For this study, we use a grid spacing of 4° latitude by 1-km altitude. A standard model simulation with this resolution takes 15 min of clock time per model year to solve for all constituents as discussed below.

[17] Time-dependent surface boundary conditions from *WMO* [2007] are specified for 1950–2005 for the following source gases: N_2O, CH_4, CO_2, $CFCl_3$, CF_2Cl_2, CCl_4, CH_3Cl, CH_3CCl_3, CH_3Br, $CBrF_3$, CF_2ClBr, $CHClF_2$, $C_2Cl_3F_3$, $C_2Cl_2F_4$, C_2ClF_5, CH_3CCl_2F, CH_3CClF_2, $CHCl_2CF_3$, and $C_2Br_2F_4$. Surface boundary conditions for CO are specified to be 150 ppbv in the Northern Hemisphere (NH) and 50 ppbv in the Southern Hemisphere (SH), with the H_2 surface boundary conditions set to 500 ppbv for all latitudes. The CO and H_2 boundary conditions are held constant with time. Water vapor is computed as described in the study of *Fleming et al.* [1995], with lower tropospheric values set to the climatology of *Oort* [1983]. For this study, we also constrain the flux of water vapor into the stratosphere by setting H_2O in the tropical upper troposphere (30°S–30°N, 11–17 km) to a seasonally varying climatology (yearly repeating) based on measurements from the Halogen Occultation Experiment (HALOE) instrument onboard UARS. HNO_3 is transported and computed separately from the other NO_y species. A diurnal average chemical production and loss computation is performed for the 19 source gases, CO, H_2, H_2O, HNO_3, HF, and CF_2O. Solid H_2O and solid HNO_3 are computed once per day following the study of *Considine et al.* [1994].

[18] To solve for the fast chemical constituents, our model now uses the scheme developed for the AER two-dimensional model [*Ko et al.*, 1984; *Weisenstein et al.*, 1991, 2004]. A diurnal cycle is computed for 35 constituents which are grouped into seven chemical families. These include: (1) O_3; (2) $O(^3P)$, $O(^1D)$, and $O_2(^1\Delta)$; (3) H, OH, HO_2, and H_2O_2; (4) N, NO, NO_2, NO_3, N_2O_5, HO_2NO_2, and HONO; (5) Cl, ClO, ClO_3, OClO, Cl_2, Cl_2O_2, $ClNO_2$, $ClONO_2$, HOCl, and HCl; (6) Br, BrO, Br_2, $BrONO_2$, BrCl, HOBr, and HBr; and (7) CH_2O, CH_3O_2, and CH_3OOH. Ten equal-length time steps are computed during the day, five equal-length time steps are computed during the night, and very short time steps are computed at sunrise and sunset. The 35 constituents are solved simultaneously at each time step using an iterative Newton/Raphson scheme. The gas phase and heterogeneous reaction rates and photolytic cross-sections are taken from the Jet Propulsion Laboratory (JPL) 2002 recommendations [*Sander et al.*, 2003], with the cross-sections for NO photolysis taken from the study of *Minschwaner and Siskind* [1993]. These rates are updated once per 24-hour period. We also specify a latitude and seasonally varying surface boundary condition for O_3 based on a climatology compiled from ground-based data averaged over 1988–2002 [*McPeters et al.*, 2007].

[19] Following the diurnal cycle computation, the diurnal average of all 62 constituents (35 fast constituents, 19 source gases, and CO, H_2, H_2O, HNO_3, HF, CF_2O, solid H_2O, and solid HNO_3) is transported separately. This is a change from our previous methodology in which chemical families were transported instead of the individual species [*Douglass et al.*, 1989]. Transporting all constituents separately is more consistent with the real atmosphere and results in only a small (~10%) increase in computational time. The major differences in the simulations occur during winter-spring at high latitudes, in which the fast chemical species (for example,

HCl, $ClONO_2$: Figure 4) are in better agreement with observations when transported individually. Total column ozone shows a general increase of 5–10 DU at winter-spring high latitudes with this new methodology. This is likely due to increased atomic oxygen in these regions (which leads to increased ozone via reaction with O_2) when all constituents are transported separately, as compared with a simulation in which only the odd oxygen family is transported. Also, the chlorine and bromine species show a greater degree of activation within the spring Antarctic vortex with this new scheme. As a result, the ozone hole occurs ~1 week earlier and is 10–20 DU deeper, thereby bringing the model into better agreement with the data (for example, Figure 6).

[20] For the transport, the coefficients for diffusion (K_{yy}, K_{yz}, and K_{zz}) and advection by the residual circulation ($\bar{v}^*$, $\bar{w}^*$) are updated once per day before being applied to the model chemical constituents. To accommodate the rapid vertical transport in the mesosphere, we use a time step of 4 hours for advection and a shorter time step of 1.5 hours for the diffusive transport throughout the model domain. We also apply rainout once per day to the following constituents: HNO_3, HCl, HBr, HF, CF_2O, H_2O_2, CH_2O, and CH_3OOH. The rainout timescale is 1–2 days in the lower troposphere and increases with height to ~1000 days at the tropopause.

[21] For the model simulations presented in this study, we use time-dependent aerosol loading for 1979–2001 from the data set utilized for *WMO* [2007]. These data include, among others, aerosol loading from the major volcanic eruptions of El Chichon in 1982 and Pinatubo in 1991. We use 1979 values for years prior to 1979 and 2001 values for years after 2001: these represent clean stratospheric aerosol conditions. We also include a parameterization to account for the 11-year solar cycle variation in UV flux using the F10.7-cm index as a transfer standard starting from fits to the UARS/Solar UV irradiance reference spectrum (SUSIM) data [*Jackman et al.*, 1996]. We do not include solar proton events or variations in galactic cosmic rays in the simulations as these have small impacts on total ozone [e.g., *Jackman et al.*, 1996].

2.3. Model Treatment of Longitudinal Variations

[22] Previously, longitudinal temperature variations were accounted for in our two-dimensional model only in the calculation of polar stratospheric cloud formation, utilizing a multiyear average longitudinal temperature probability distribution computed from NCEP data [*Considine et al.*, 1994]. Zonal mean temperatures were used to compute the gas phase and heterogeneous reaction rates. In light of other two-dimensional model results illustrating the importance of accounting for longitudinal temperature variations in the model chemistry [*Smyshlyaev et al.*, 1998; *Solomon et al.*, 1998; *Weisenstein et al.*, 1998], we have incorporated a new scheme to account for this zonally asymmetric variability while maintaining the computational speed of the two-dimensional model framework.

[23] This methodology uses an off-line parcel trajectory model input with winds and temperatures from the meteorological analyses and is described as follows. Given that the reaction rates and polar stratospheric cloud (PSC) surface area are computed once per day in our model, we seek to determine what temperatures are experienced at each model grid point (4° × 1-km resolution) over the course of 1 day. To do this, parcels are initialized at every 2.5° longitude around each model latitude and are then advected backward for 12 hours and forward for 12 hours. From this we construct a temperature probability distribution at 1-K increments. The gas phase and heterogeneous reaction rates and PSC surface area at each model grid point are then computed each day by summing the respective values computed at each temperature in the distribution weighted by the probability of occurrence of that temperature. To greatly reduce the computational and memory requirements of the two-dimensional model while maintaining most of the variability of interest, we use 5-day averages of winds and temperatures instead of daily data to generate the probability distributions. For this study, we performed these calculations for all years available in each meteorological data set, for example, the NCEP data for each year, 1958–2004.

[24] Including this new treatment of temperature variability in the heterogeneous reaction rates accounted for more of the inherent nonlinearity of these reactions and reduced total column ozone at all latitudes and seasons compared with using only the zonal mean temperatures. Ozone reductions were largest in the high-latitude late winter and spring following major volcanic eruptions when the stratospheric sulfate aerosol loading was largest. In the NH, these reductions were relatively small, ~2–4 Dobson Units (DU). At SH high latitudes, ozone decreases were much larger: reductions of 7 DU and 20 DU occurred during October 1984 following El Chichon and in October 1992 following Pinatubo, respectively. Ozone was also systematically reduced by ~10 DU in the SH late winter-spring high latitudes during the period of large halogen loading after the mid-1990s. However, using this new methodology in the gas phase reactions had a very small effect. The changes in total ozone were at most ±1–2 DU at winter high latitudes and <±1 DU at low latitudes.

[25] In a similar fashion, we used the same parcel trajectory model to provide a correction to the solar insolation used to compute the model photolysis rates. For this, we constructed a distribution of latitudes and, hence, solar zenith angles at 1° increments, that parcels experience over the course of 1 day. The photolysis rates at each two-dimensional model grid point are then computed each day by summing the rates at each latitude in the distribution weighted by the probability of occurrence of that latitude. This method then represents a correction to the standard method (i.e., just using the single "zonal mean" latitude). The result is generally an increase in ozone at most levels because of the fact that this insolation correction effectively increases the ozone production at a greater rate than the increase in the ozone loss [e.g., *Jackman and McPeters*, 1985]. The change in total column ozone is always positive, with maximum increases of 4–5 DU occurring in the polar early spring of both hemispheres where parcels undergo large excursions from their reference latitudes near the polar night terminator. At lower latitudes, only very small changes in total column ozone occur (<1 DU).

[26] While this insolation correction always results in an increase in total column ozone, there are decreases in the ozone profile at 15–22 km during the Antarctic spring caused by the perturbed chemistry of the ozone hole. Here the increased insolation leads to increased chlorine activa-

tion via heterogeneous reactions on NAT and ice PSCs. This effect is most pronounced during years with an especially isolated vortex, cold temperatures, and a deep ozone hole (for example, October 1987, 2001). Similarly, we also obtain a high-latitude ozone decrease at 15–22 km during the very cold NH late winter-spring of March–April 1997.

3. Statistical Regression Analysis

[27] For this study, we will focus on the 1979–2004 time period for which satellite-based total ozone data are available. We will show results obtained from statistical regression analysis on the observed and modeled total ozone time series similar to that done in previous studies [e.g., *Stolarski et al.*, 1991, 2006; *Ziemke et al.*, 1997]. The regression model consists of the long-term mean and the first four seasonal harmonics to represent the seasonal cycle. Additional terms are used to represent the time-dependent halogen changes, the major volcanic eruptions of El Chichon in 1982 and Pinatubo in 1991, the 11-year solar cycle variations, and the QBO. These additional terms are fit with an annual mean and seasonal harmonics.

[28] The halogen term is represented by the total inorganic chlorine mixing ratio plus 50 times the total inorganic bromine mixing ratio from model simulations at 1 hPa. This represents the effective chlorine loading in the stratosphere as discussed in the study of *Stolarski et al.* [2006]. Terms describing the stratospheric aerosol changes due to the El Chichon and Pinatubo eruptions are fit using separate chemical-transport model simulations of the aerosol effects only. The solar cycle fit is proportional to the 10.7-cm radio flux measured at Ottawa, Canada.

[29] The QBO term is represented following the methodology outlined previously, utilizing the two leading empirical orthogonal functions (EOFs) of the zonal wind QBO reference time series [*Wallace et al.*, 1993; *Randel and Wu*, 1996; *Randel et al.*, 1999]. This time series is derived from optimal linear combinations of near-equatorial radiosonde observations of zonal wind for 70–10 mbar. Together, these two leading EOFs explain more than 90% of the QBO zonal wind variance [*Wallace et al.*, 1993; *Randel et al.*, 1999]. This technique therefore isolates variations in the total ozone time series that are coherent with the equatorial zonal wind QBO.

4. Model Comparisons With Climatological Tracer Data

[30] Previous studies have presented an extensive evaluation of our empirically based model dynamics using a multiyear climatological average of the transport fields [*Fleming et al.*, 1999; *Hall et al.*, 1999]. These studies showed that the model gives good agreement with a variety of ozone and long-lived tracer measurements in simulating transport-sensitive features, including the age of air and seasonal cycle propagation in the tropics. We now present a brief overview of these model-data comparisons utilizing the model transport fields that have been updated to account for interannual variability as discussed in section 2.

[31] Here and in the following sections, we will show results from several model sensitivity simulations which include various combinations of the input parameters (halogen and aerosol loading, solar cycle variations, and interannual dynamical variability). These model simulations are summarized in Table 1.

Table 1. List of Model Simulations

Simulation	Atmospheric Perturbations Included
A	Time-dependent halogen loading Time-dependent stratospheric sulfate aerosol loading 11-year solar cycle UV flux variations Interannual transport and temperature variability from NCEP data
B	As in A, but with interannual transport and temperature variability from ERA-40 data
C	Time-dependent halogen loading Yearly repeating climatological transport and temperature from NCEP data
D	Time-dependent halogen loading Time-dependent stratospheric sulfate aerosol loading Yearly repeating climatological transport and temperature from NCEP data
E	Time-dependent halogen loading Time-dependent stratospheric sulfate aerosol loading 11-year solar cycle UV flux variations Yearly repeating climatological transport and temperature from NCEP data
F	11-year solar cycle UV flux variations Yearly repeating climatological transport and temperature from NCEP data
G	Interannual transport and temperature variability only, from NCEP data
H	Interannual transport and temperature variability only, from ERA-40 data

4.1. Age of Air

[32] Stratospheric age of air is a widely used diagnostic that tests the overall fidelity of model transport [*Hall and Plumb*, 1994; *Hall et al.*, 1999]. Figure 1 shows the mean age of air at 20 km and vertical age profiles at three latitude zones from model simulations using transport fields derived from both sets of meteorological data (simulations A and B). The modeled age of air is averaged over the 1990s and is compared with ages derived from aircraft measurements of SF_6 and CO_2 at 20 km, and a series of vertical profile measurements of SF_6 and CO_2 made from balloon flights at various latitudes [e.g., see *Hall et al.*, 1999]. The age of air in the model is computed from a "clock" tracer that has a surface boundary condition linearly increasing with time, with no other chemical production or loss. This is essentially identical to the age obtained from simulations of SF_6 or CO_2, as done, for example, in *Hall et al.* [1999].

[33] There can be some significant differences in the observations at the middle and higher latitudes. Some of this may be due to possible photochemical influences on SF_6 which would cause an overestimation in the inferred ages [*Hall and Waugh*, 1998]. Some of the older age measurements at 65°N may also reflect remnants of the winter polar vortex [*Ray et al.*, 1999] which cannot be resolved in the two-dimensional model. Nevertheless, the models compare well with the data overall, including the absolute values and the latitudinal and vertical gradients. At 20 km, both models are within the range of the observations, although model B (based on the ERA-40 meteorology) tends to be on the old side of the data at most latitudes. This result is in contrast with the known problem of an excessively strong Brewer-Dobson circulation and a younger age of air in the ERA-40 reanalyses as reported by *Uppala et al.* [2005].

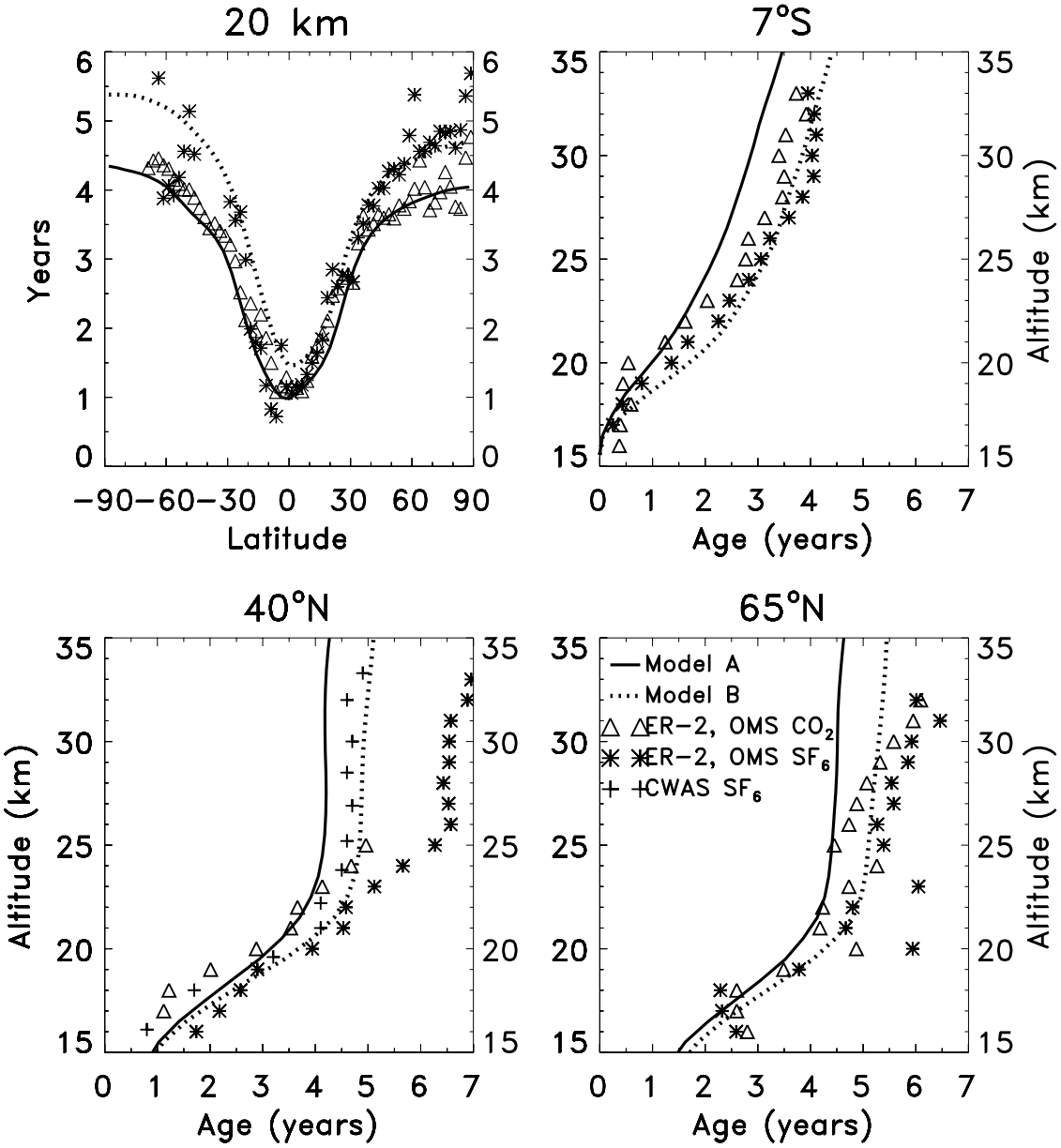

Figure 1. Age of air at 20 km derived from ER-2 aircraft measurements of SF_6 (asterisks) and CO_2 (triangles) and vertical profiles of the age of air derived from balloon measurements of SF_6 (asterisks, plus signs) and CO_2 (triangles) at the latitudes indicated. Ages derived from these measurements have been adapted from *Hall et al.* [1999]. Also shown are model simulations A and B using transport derived from the two sets of meteorological data indicated in Table 1. The age is taken relative to the tropical tropopause.

[34] In the vertical profiles, both models are within the observed range below ~24 km. Above ~24 km, model A (based on the NCEP data) is close to or a bit younger than the observations, while model B tends to be on the old side of the data. Maximum differences of ~1 year occur between the two simulations at the higher latitudes and above 25 km. While this difference in age appears to be significant, it is due to rather small differences in the transport fields, especially in the lower stratospheric vertical diffusion in which the K_{zz} derived from the ERA-40 data is slightly smaller than that derived from the NCEP meteorology. However, we found that the resulting impact of these K_{zz} differences on the total ozone simulations was rather small.

4.2. H_2O and CH_4

[35] As further evaluation of the model transport, we show latitude-height cross-sections of March H_2O (Figure 2) and September CH_4 (Figure 3) from model A and UARS/HALOE data, both averaged over 1994–2004. The simulations of these tracers do not show significant differences between the two sets of meteorological data, and we show results using transport derived from the NCEP data in model A in Figures 2 and 3.

[36] Again, the model shows good overall agreement with the data in reproducing transport-sensitive features in the meridional plane, including the horizontal and vertical

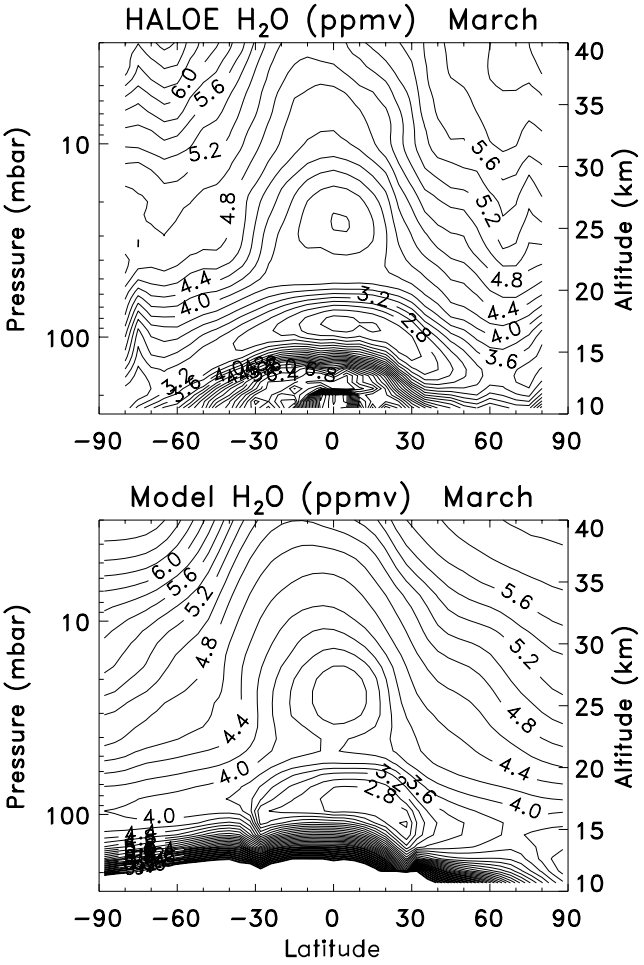

Figure 2. Latitude-height cross-sections of March H_2O averaged over 1994–2004 from UARS/HALOE (top) and model simulation A (bottom). Contour interval is 0.2 ppmv.

gradients [e.g., *Holton*, 1986]. The model captures the tropical isolation in the lower stratosphere, as indicated by strong horizontal gradients in the subtropics, and a "bubble" of low water vapor concentrations at 20–30 km associated with the "tape recorder" signal [e.g., *Mote et al.*, 1996]. The model also qualitatively simulates the region of strong horizontal mixing during late winter/early spring at midlatitudes. This is especially pronounced in the SH during September at 20–40 km in the CH_4 field.

[37] Note also that the HALOE H_2O data indicate strong poleward and downward transport of very dry air from the tropics to midlatitudes just above the tropopause [e.g., *Randel et al.*, 2001]. The model, which includes the off-diagonal eddy mixing term projecting this rapid horizontal transport onto isentropic surfaces (section 2.1), shows qualitative consistency with the HALOE data in resolving this feature. However, the simulation tends to underestimate the downward penetration of this feature at high latitudes. Some of this discrepancy is likely due to inadequate model representation of moist processes related to convection (for example, rainout, etc.), and limitations of a two-dimensional model in simulating transport processes in this region may also be a factor. However, as discussed in the next section, the model representation of ozone in this region appears to be quite reasonable.

4.3. HCl and $ClONO_2$

[38] To give a broad comparison of the chemical constituents related to ozone depletion, Figure 4 shows the monthly averaged HCl from UARS/HALOE (top panel, black solid line) along with $ClONO_2$ (bottom panel, black solid line) from the Cryogenic Limb Array Etalon Spectrometer (CLAES) instrument onboard UARS, both for April 1993. The corresponding values from model simulation A are shown in the red dashed contours, and we found the comparisons for other seasons to be similar to that shown in Figure 4. The model $ClONO_2$ is in mostly good agreement with the CLAES data. The simulation mostly reproduces the latitudinal and vertical gradients, and there does not appear to be any systematic bias in the absolute amounts of $ClONO_2$.

[39] The simulation of HCl is also in mostly good agreement with the HALOE data in reproducing the latitudinal and vertical gradients. The model tends to overestimate the HALOE absolute values by as much as 0.2–0.4 ppbv. However, previous studies have noted that compared with

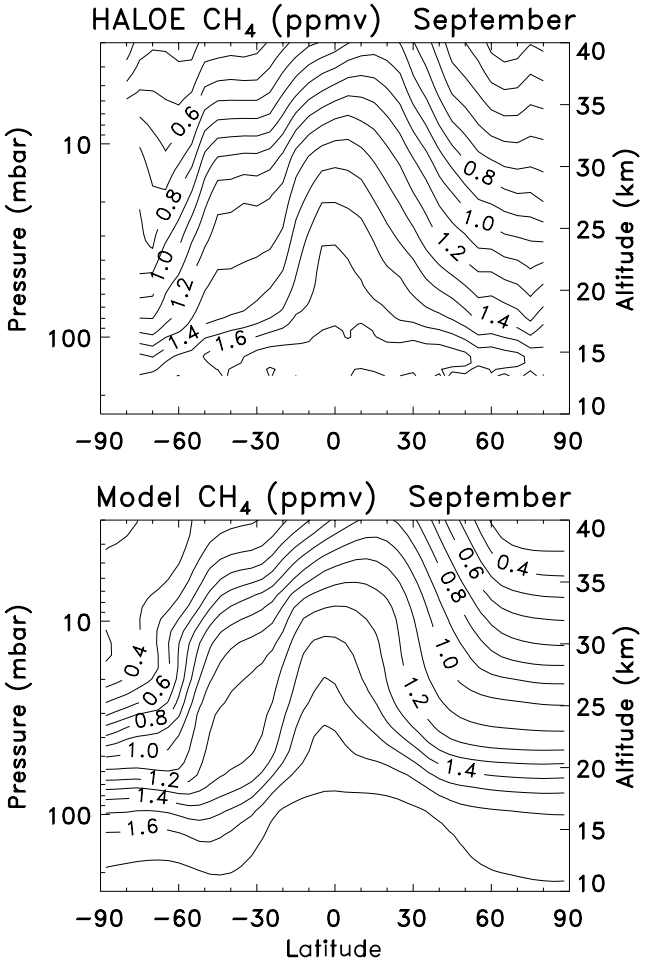

Figure 3. Latitude-height cross-sections of September CH_4 averaged over 1994–2004 from UARS/HALOE (top) and model simulation A (bottom). Contour interval is 0.1 ppmv.

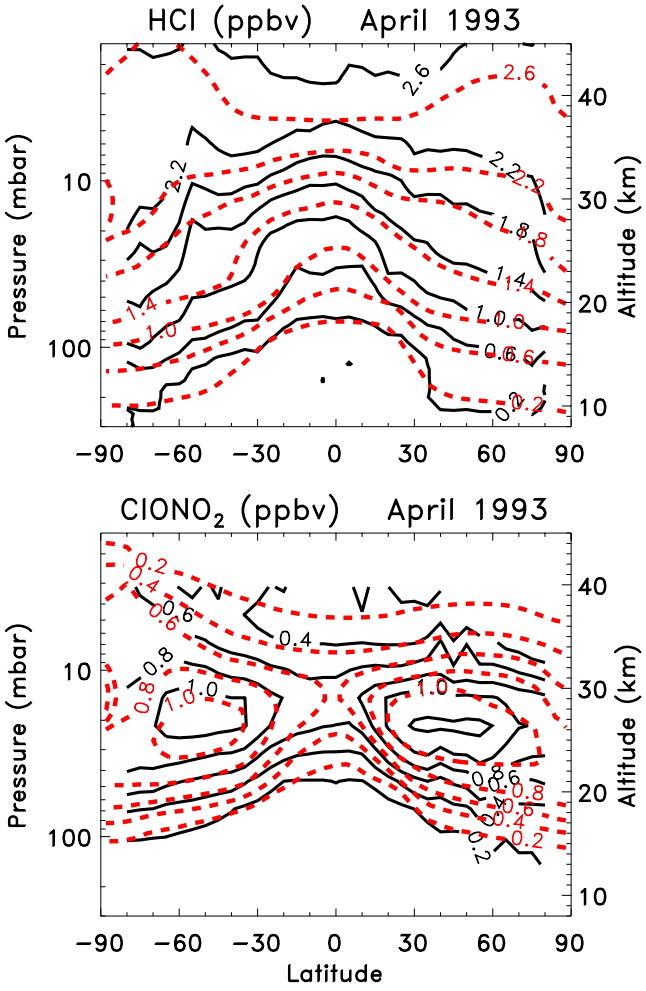

Figure 4. Latitude-height cross-sections of monthly averaged HCl from UARS/HALOE (top, black solid line) and $ClONO_2$ from UARS/CLAES (bottom, black solid line) for April 1993. The dashed red line contours show the corresponding values for model simulation A. The contour interval is 0.4 ppbv for HCl and 0.2 ppbv for $ClONO_2$.

measurements from the MLS instrument onboard the Earth Observing System (EOS) Aura satellite and the Atmospheric Chemistry Experiment (ACE), HALOE HCl values are smaller by ~10%–15% (0.2–0.4 ppbv) at most levels of the stratosphere [e.g., *Froidevaux et al.*, 2006]. This implies that the model HCl values, while overestimating HALOE, are probably close to those other measurements. This, along with the good agreement in $ClONO_2$, suggests that the model chlorine chemistry in the stratosphere is quite reasonable.

4.4. Ozone

[40] Previous studies have shown that total column ozone, being a vertically integrated quantity, can be reasonably well simulated even with significant discrepancies in the model transport fields [e.g., *Park et al.*, 1999]. Therefore it is important to evaluate the model simulations of the ozone vertical profile, especially in the 10- to 25-km region where ozone is highly sensitive to transport and the ozone profile has the largest contribution to the total column. Figure 5 shows latitude-height cross-sections of annually averaged ozone from an observational monthly mean climatology (top panel), model simulation A (middle panel), and the difference, model minus data (bottom panel) expressed in DU per kilometer. This unit is proportional to the number density per cm^2 divided by a constant and is a direct measure of the contribution versus altitude to the total column. The climatology is based on a combination of ground-based and satellite data covering the time period 1988–2002, as compiled by *McPeters et al.* [2007]. The model results are also averaged over 1988–2002.

[41] The simulation compares relatively well with the data in most regards. The model qualitatively reproduces the observed latitudinal and vertical gradients in most places, as well as the magnitude of the ozone amounts. The model does show an overestimation of ozone at 15–22 km at

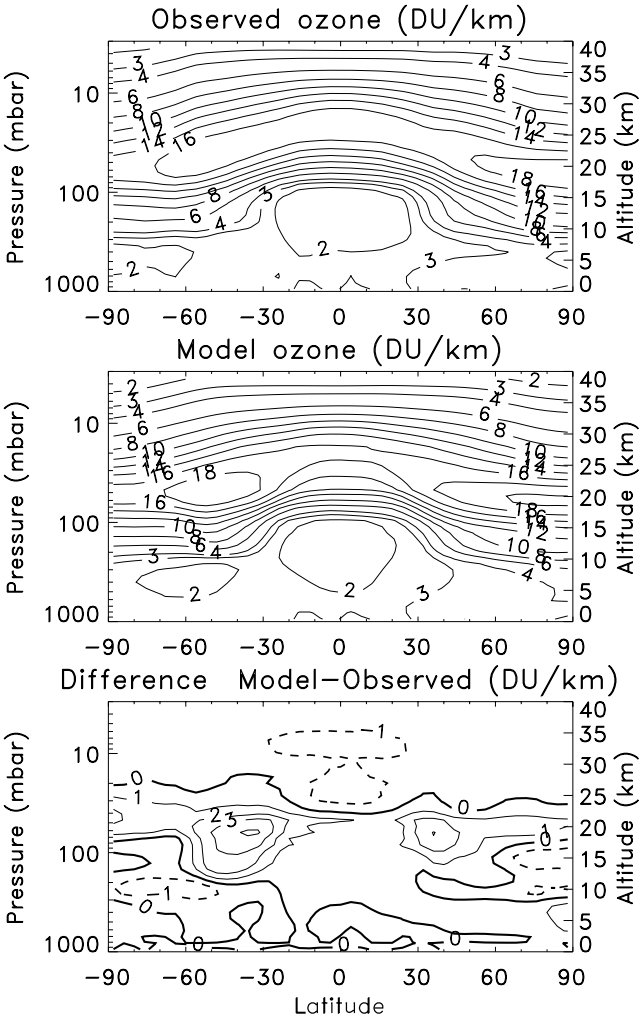

Figure 5. Latitude-height cross-sections of annually averaged ozone expressed in Dobson Units per kilometer. The observations (top panel) are from the climatology compiled by *McPeters et al.* [2007] covering the time period 1988–2002. Also shown are model simulation A averaged over 1988–2002 (middle panel) and the difference, model minus observations (bottom panel). For the top and middle panels, the contour interval is 2 DU/km and includes the 3 contour level. The contour interval is ±1 DU/km for the bottom panel.

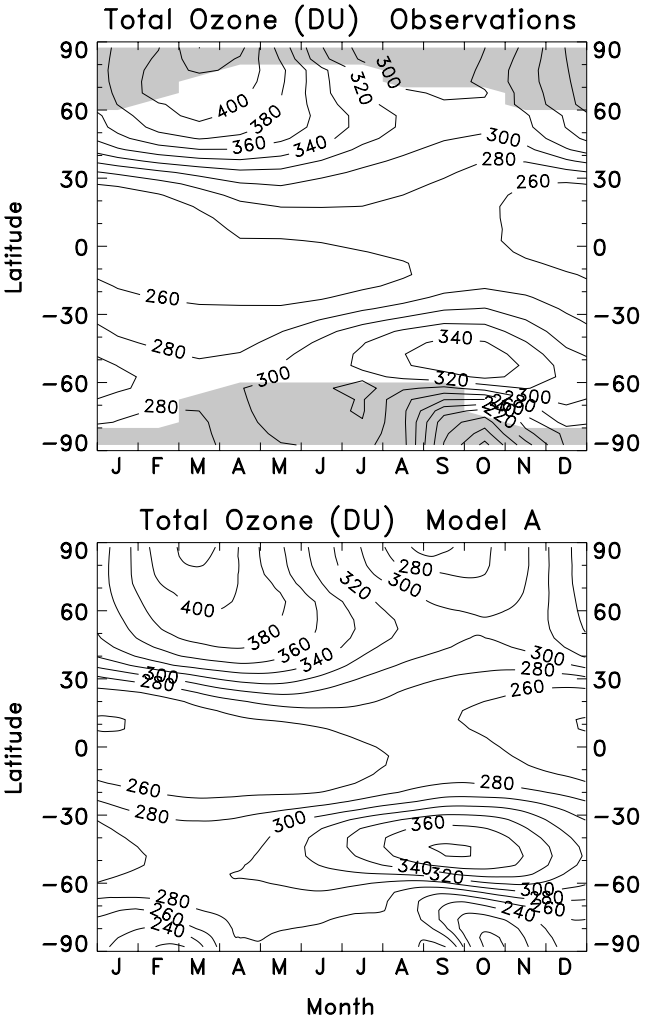

Figure 6. Month-latitude cross-sections of total column ozone averaged over 1988–2002 from observations (top panel) and model simulation A (bottom panel). Outside of polar night, the observations are from the TOMS/SBUV merged ozone data set. As denoted by the shading, the observations in polar night are derived by vertically integrating the ozone climatology compiled by *McPeters et al.* [2007]. The contour interval is 20 DU.

midlatitudes of both hemispheres and a general underestimation of ozone at 25–35 km mainly in the tropics. However, given the model improvements discussed in section 2, these differences are significantly smaller than obtained in previous model versions [*Fleming et al.*, 2002], and the magnitudes of the horizontal and vertical gradients are now in significantly better agreement with the data. We note that differences in the lower troposphere are quite small given that the model ozone is tied to the climatology at the surface (section 2.2).

[42] The corresponding season-latitude sections of total column ozone also averaged over 1988–2002 are shown in Figure 6. The observations outside of polar night are from the TOMS/SBUV merged total ozone data set (MOD) [*Stolarski et al.*, 2006]. For completeness in the winter polar region where the TOMS/SBUV data are missing, we have included, as denoted by the shading, total ozone data derived by vertically integrating the ozone climatology compiled by *McPeters et al.* [2007]. For visual clarity when merging the two data sets in the contour plot, we have slightly reduced the vertically integrated column ozone data in the shaded region by 5%, which is within the uncertainty of the ozone profile climatology (G. Labow, private communication, 2006).

[43] Again, the model shows good overall agreement with the data. Consistent with Figure 5, midlatitude total ozone tends to be overestimated somewhat in the model, especially in the SH. The temporal duration and depth of the Antarctic ozone hole also are underestimated in the model, and this is likely due to limitations of the zonal mean framework in simulating polar heterogeneous processes deep within the vortex (poleward of 80°S) as discussed in section 6.2.

[44] Latitudinal profiles of the long-term mean and seasonal cycle amplitude and phase of total ozone derived from the regression analysis for 1979–2004 are shown in Figure 7 for 60°S–60°N. Shown are the TOMS/SBUV MOD data (black line) and results from the model simulations using the two sets of meteorological data as indicated

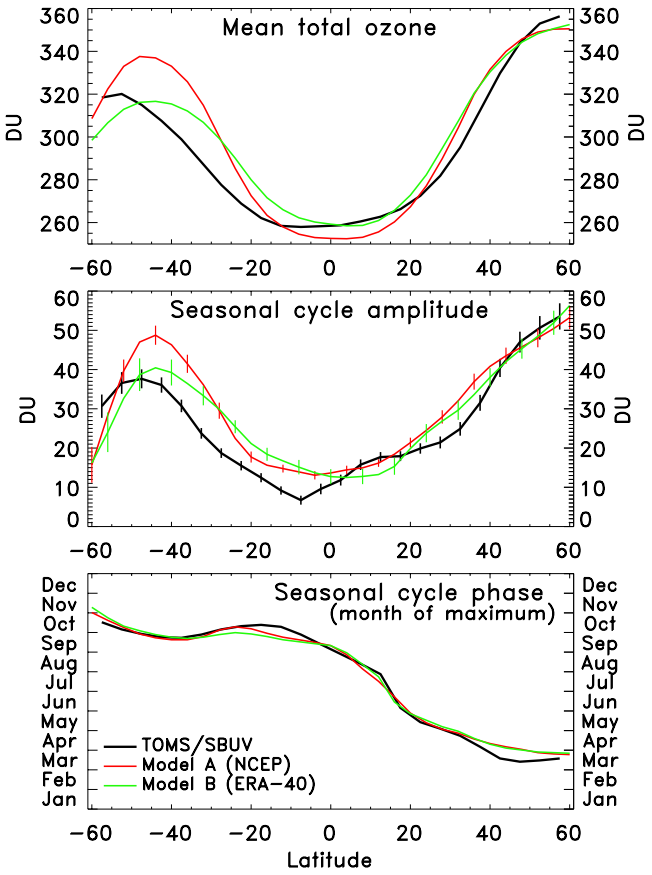

Figure 7. Latitude profiles of the average value of total ozone (DU), and the seasonal cycle amplitude (DU, taken as one-half the maximum minus minimum ozone over the course of 1 year) and phase (time of maximum), for 1979–2004 obtained from the regression analysis. Shown are the results for the TOMS/SBUV merged total ozone data (black line) and model simulations A (red line) and B (green line), which use the meteorological data as indicated. Also shown are the 2σ uncertainty bars on the seasonal cycle amplitude.

(simulations A and B). The 2σ uncertainty bars on the seasonal amplitude are related to the variance of the seasonal cycle obtained from the regression at each latitude for the 26-year time period. The simulations capture many of the observed characteristics, including the overall latitudinal variations. The models underestimate the latitudinal extent of the region of flat mean ozone gradients observed in the tropics so that there is a general model overestimation of the mean ozone in the subtropics and midlatitudes of the SH, especially in model A. The resulting near-global average (60°S–60°N) total ozone for 1979–2004 is overestimated by 7 DU in the models: 287 DU for the observations versus 294 DU for both model A and model B.

[45] The seasonal cycle phase of the models compares well with the data at most latitudes. The simulated seasonal amplitude is mostly within the 2σ uncertainty of the observations northward of the equator. However, the simulations overestimate the observed seasonal amplitude at 5°S–45°S. Also, the data show a rather strong low-latitude asymmetry about the equator, with the seasonal amplitude at 7°N–15°N being twice as large as that at 7°S–15°S. A similar, although weaker asymmetry is also seen in the long-term mean ozone data (top panel). Model A (red line) shows some indication of this asymmetry in the seasonal amplitude, although much weaker than observed.

[46] Overall the models compare reasonably well with the data in reproducing the absolute total ozone magnitudes, the latitudinal gradients, and the seasonal variations. The good overall model agreement with the observations in Figures 5, 6, and 7 gives us confidence that the simulations of the perturbations introduced into the ozone field will yield reasonable results.

5. Interannual Variability in Total Ozone

[47] Figure 8 shows 1979–2004 time series of deseasonalized total ozone from the TOMS/SBUV MOD data set and model simulations A and B for the latitude zones indicated. The time series have been deseasonalized by removing the mean and seasonal cycles shown in Figure 7. Again, these simulations contain time-dependent source gas boundary conditions and stratospheric aerosol loading, the 11-year solar cycle variations in UV flux, and interannually varying transport and temperature fields derived from the two sets of meteorological data (Table 1).

[48] In the near-global average, the models do a reasonable job in qualitatively resolving the observed year-to-year oscillations throughout the time series, including the QBO-like features. The large observed drop-off during 1991–1993 associated with the aerosol enhancement following the Pinatubo eruption is also reproduced, although the simulated magnitude is underestimated.

[49] The QBO-like variations dominate the observed time series at NH midlatitudes. Although the models reproduce these features for the most part, the observed sharp drop-offs during early 1993 and early 1995 are underestimated in the simulations. At SH midlatitudes, the observed QBO variations are not quite as consistent throughout the time period compared with the NH data. Although the sparse coverage of radiosonde data in the SH may reduce the quality of the met analyses compared with the NH, model A (based on the NCEP data)

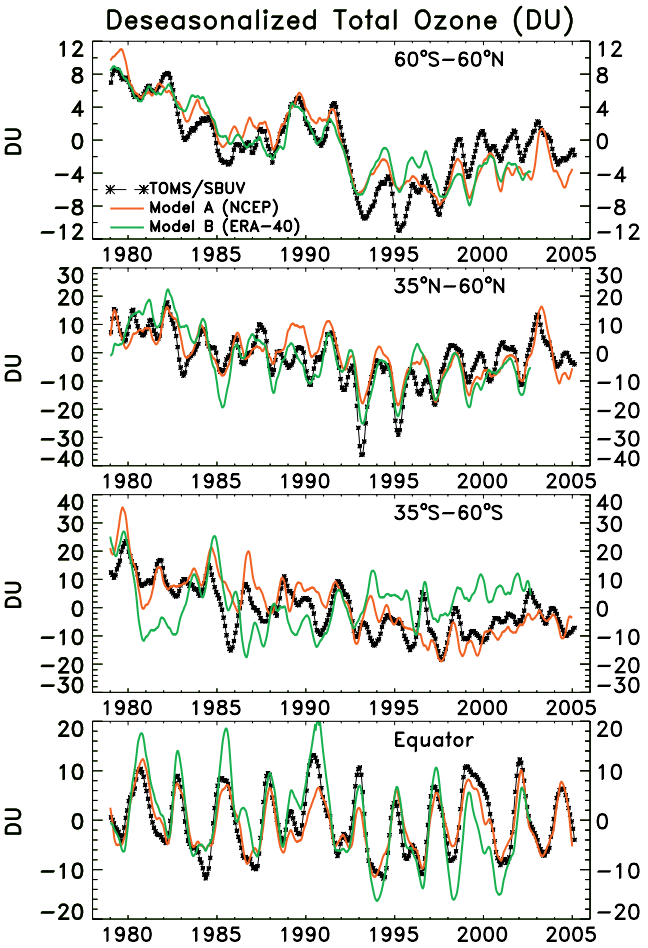

Figure 8. Time series of deseasonalized total ozone at different latitude zones from the TOMS/SBUV merged ozone data set (black dashed-asterisk), and model simulations A (red line) and B (green line) which use the meteorological data as indicated.

compares reasonably well with the total ozone observations at SH midlatitudes. However, the ERA-40-based model (model B) reveals some larger discrepancies with the data in the SH. For example, this model underestimates the observed anomalies for 1980–1983 and 1986–1990 and mostly overestimates the observed anomalies during 1993–2002. Also, both models A and B underestimate the large observed ozone drop-off during 1985 in the SH. At the equator, the well-known large QBO-induced oscillations dominate throughout time period. Both models capture the phase of this feature rather well, although the amplitude of the ERA-40-based model is noticeably larger than simulated by the NCEP-based model.

[50] Figure 9 shows the root mean square deviations from the mean (RMS), as a function of month and latitude, of the total ozone time series shown in Figure 8. The models generally pick up the observed seasonality, with large RMS amplitudes during the high-latitude winter and spring of both hemispheres. In the NH, this is due mainly to the large year-to-year changes driven by fluctuations in planetary wave activity. In the SH, the large high-latitude RMS values

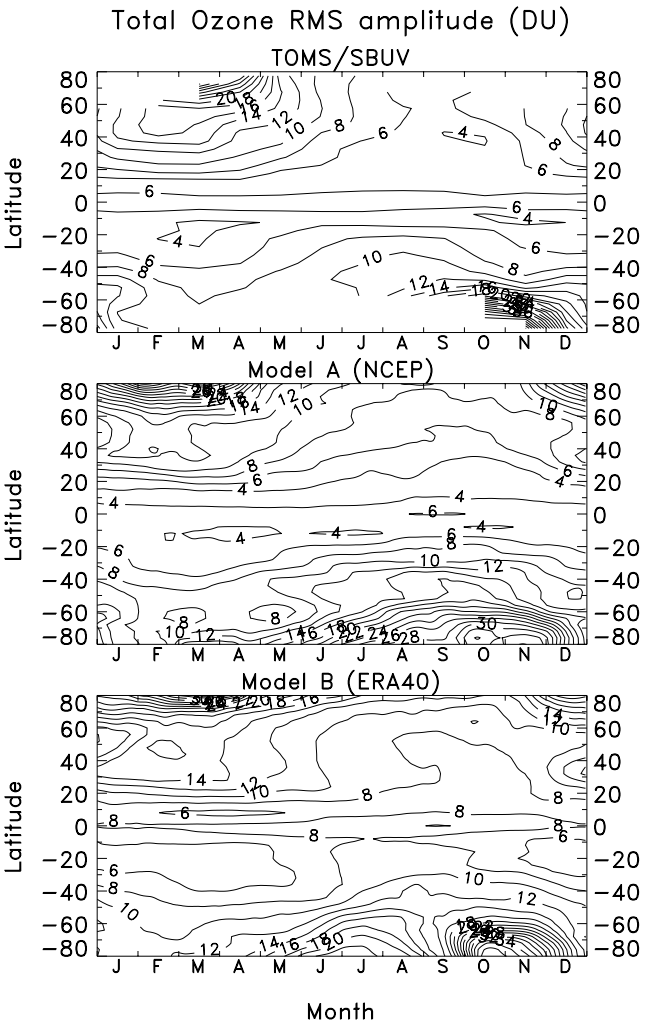

Figure 9. Root mean square deviations from the mean of total ozone as a function of month and latitude. Values are derived from the 1979–2004 time series of the TOMS/SBUV merged ozone data set (top), and model simulations A (middle) and B (bottom) which use the meteorological data as indicated. Contour interval is 2 DU.

during September–October are driven largely by the strong downward trend within the Antarctic ozone hole due to the increased halogen loading. During November in the SH polar region, there are large interannual variations because of dynamical changes, as will be discussed in section 6.2. Relatively small RMS values occur during the summer and early fall of both hemispheres. While both models are qualitatively consistent with the data, the ERA-40-based model has generally larger RMS amplitudes during most months and latitudes compared with the NCEP-based model, as was seen in Figure 8.

[51] Figure 10 shows latitudinal profiles of the annually averaged equivalent harmonic amplitude and phase of the QBO signals in total ozone. These are computed from the two leading QBO EOFs in the regression analysis (section 3), similar to the methodology outlined in *Wallace et al.* [1993]. Again, the 2σ error bars provide a measure of the variance of the QBO signal at each latitude over the 26-year time period. The TOMS/SBUV data show the well-known peak in amplitude of 8 DU at the equator, with a sharp drop-off to small amplitudes in the subtropics (10°–15°) of both hemispheres. There is a secondary amplitude maximum of ~6 DU at midlatitudes of both hemispheres, which is roughly one-half of a QBO cycle out of phase with the equatorial oscillation. These features have been discussed previously and are related to latitudinal variations in the meridional circulation associated with the QBO [e.g., *Gray and Pyle*, 1989; *Hasebe*, 1994; *Jones et al.*, 1998; *Randel et al.*, 1999; *Kinnersley and Tung*, 1999; *Huesmann and Hitchman*, 2001; *Baldwin et al.*, 2001].

[52] The models generally simulate this observed latitudinal structure, with equatorial maxima, subtropical minima, and secondary maxima at midlatitudes. The NCEP-based simulation (model A) tends to underestimate the observed amplitude, while the ERA-40-based model (B) tends to overestimate the observations. However, both simulations are mostly within the 2σ uncertainty of the data, although model B does not fully resolve the subtropical minimum in the SH. The corresponding latitudinal phase variation in Figure 10 is mostly well resolved by both models, with the characteristic out-of-phase relationship simulated between

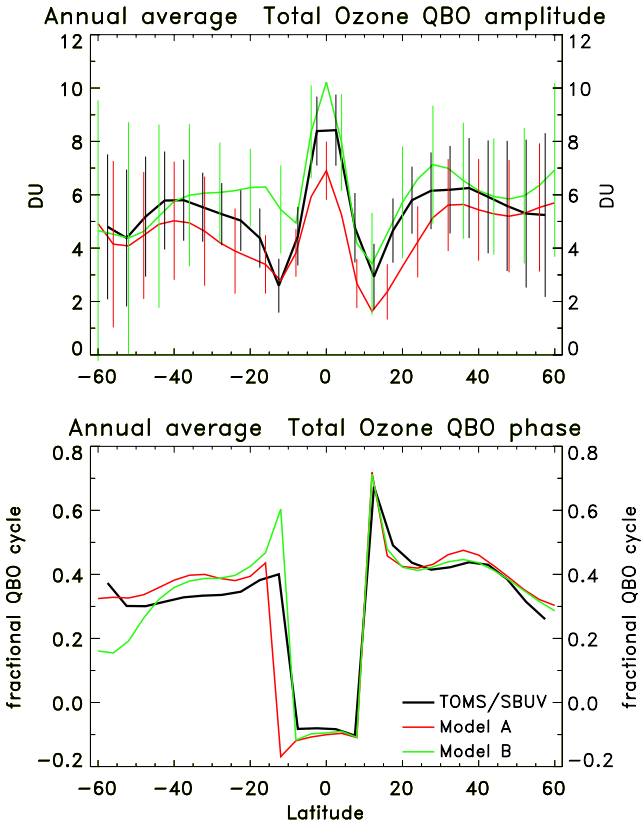

Figure 10. Latitude profiles of the annually averaged equivalent harmonic amplitude (DU) and phase (fractional cycle) of the QBO signal in total ozone for 1979–2004 derived from the regression analysis. Shown are results for the TOMS/SBUV merged ozone data set (black line), and model simulations A (red line) and B (green line) using the meteorological data as indicated in Table 1. Also shown are the 2σ uncertainty bars on the QBO amplitude. See text for details.

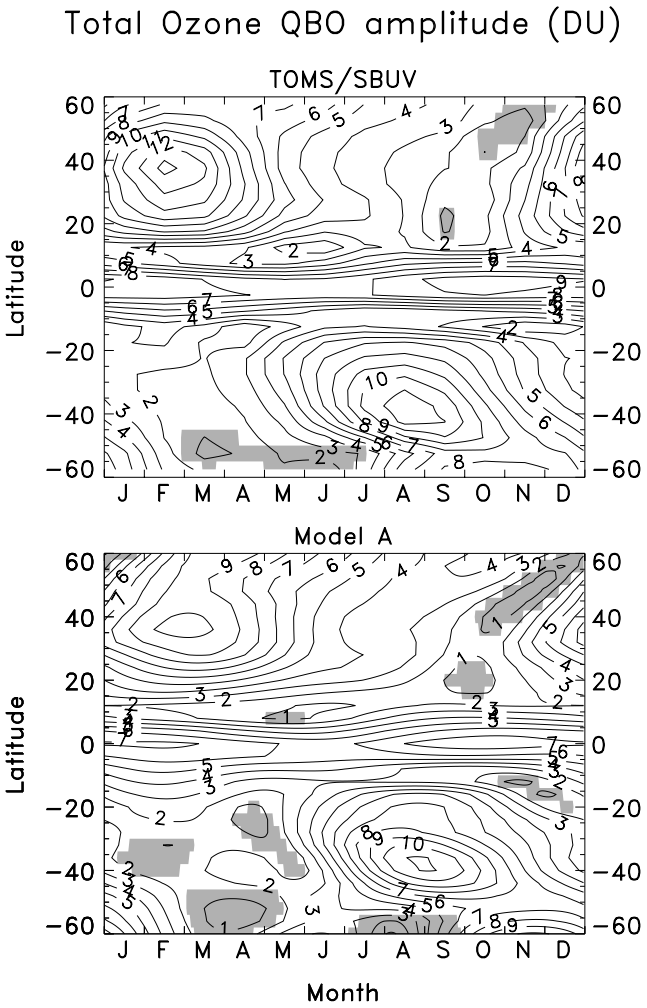

Figure 11. The equivalent harmonic amplitude of the QBO signal in total ozone as a function of month and latitude, derived from the regression analysis for 1979–2004. Shown are results for the TOMS/SBUV merged ozone data set (top panel), and model simulation A (bottom panel). The shaded areas indicate where the signal is not statistically significant at the 2σ level. The contour interval is 1 DU. See text for details.

the equatorial and midlatitude QBO oscillations of both hemispheres.

[53] As discussed in section 2.1, the model includes parameterized eddy momentum forcing from several equatorial wave sources following the methodology of *Dunkerton* [1997]. Including these processes enhances the tropical meridional QBO circulation in the model. The resulting total ozone QBO amplitude of the ERA-40-based model (B) is larger than the data at the equator in Figure 10 (see also Figure 8, bottom panel), while the NCEP-based model (A) underestimates the observed equatorial amplitude by ~15%. This latter point is consistent with previous studies showing that the NCEP reanalyses underestimate the equatorial QBO amplitude compared with the Singapore rawinsonde data [e.g., *Huesmann and Hitchman*, 2001]. However, the reanalyses capture fairly well the phase of the equatorial QBO anomalies in temperature and zonal wind. These anomalies then determine the phase of the meridional QBO circulation in the model via the anomalies in net diabatic heating and parameterized eddy momentum forcing. Therefore the resulting total ozone simulations for both models A and B show very good agreement with the observed QBO phase at the equator, as seen in Figure 10 and Figure 8 (bottom panel).

[54] Figure 11 shows the seasonality of the QBO amplitude in total ozone as a function of latitude. The data show the sharp equatorial maxima and subtropical minima in both hemispheres as seen in Figure 10. Large QBO signals are observed during late winter-spring at midlatitudes of both hemispheres, with minima during summer and fall. Similar seasonality based on Nimbus 7 SBUV total ozone data for 1979–1990 was presented in *Hollandsworth et al.* [1995]. The mechanisms responsible for the extratropical QBO and related seasonality have been discussed in previous interactive two-dimensional model studies. For example, *Kinnersley and Tung* [1998] and *Jones et al.* [1998] argue that the observed midlatitude seasonality seen in Figure 11 is due to the seasonality in the direct meridional QBO circulation anomalies which have winter maxima and summer minima. Kinnersley and Tung also found that the seasonality of the planetary wave effects on the circulation controls the total ozone seasonality at high latitudes. *Gray and Ruth* [1993] discuss the interaction of the equatorial QBO with the annual cycles in the Hadley circulation and midlatitude eddy activity in driving the QBO signals in extratropical ozone. These mechanisms appear to be well resolved by the meteorological analyses, as shown in Figure 11 (bottom). Here model A captures the observed ozone QBO seasonality quite well in both hemispheres and in the tropics. The good overall agreement seen in Figures 10 and 11 illustrates that the zonal mean transport fields determined empirically from the meteorological analyses can resolve many of the observed global QBO features in total ozone.

6. Comparison of Processes That Control Long-Term Ozone Variations

[55] We now compare in more detail the processes that control long-term ozone variations over the 1979–2004 time period. For this we will show model results that derive the yearly transport and temperature changes from the NCEP reanalyses. As seen in Figure 8, this data set provided reasonably stable long-term ozone simulations over the 26-year time period and provided the best overall consistency with the observations. The model simulation utilizing the ERA-40 data resulted in some spurious drifts in ozone due to transport variations in the SH. This model in Figure 8 (model B, green line) shows an upward trend between 1986 and 2002 at SH midlatitudes, which is significantly different from the TOMS/SBUV data [see also *Chipperfield*, 2003] and the NCEP-based model A.

6.1. Ozone Time Series, 60°S–60°N

[56] Figure 12 shows time series plots of the deseasonalized TOMS/SBUV data (asterisk-dashed line) at different latitude zones as shown in Figure 8. Also shown are four model simulations as listed in Table 1 which include the following: (1) time-dependent halogen loading with yearly repeating climatological transport and temperature fields

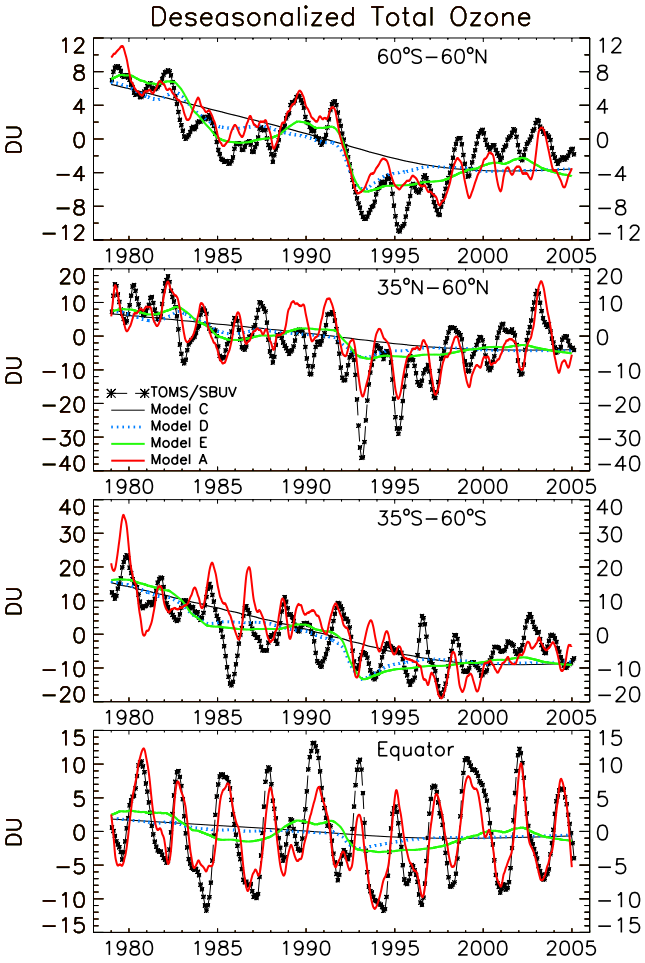

Figure 12. Time series of deseasonalized total ozone (DU) from the TOMS/SBUV merged ozone data set, and four model simulations as listed in Table 1. See text for details.

(black line, model C); (2) model C plus time-dependent stratospheric sulfate aerosol loading (blue dotted line, model D); (3) model D plus the 11-year solar cycle UV flux variations (green line, model E); and (4) model E plus interannual variability derived from the NCEP reanalyses (red line, model A, as in Figure 8).

[57] This figure illustrates the relative roles of these different processes in controlling long-term ozone changes, using the now 26-year data record to build on previous work [e.g., *Jackman et al.*, 1996; *Solomon et al.*, 1996, 1998; *Callis et al.*, 1997; *Geller and Smyshlyaev*, 2002; *Chipperfield*, 2003]. In the near-global average (60°S–60°N, top panel), much of the long-term ozone change can be attributed to the combination of halogen and aerosol loading and the solar cycle flux variations (green line). The halogen-induced decreases are ~11 DU (3.7%) from 1979 to the late 1990s, and the large decrease in ozone during 1992 following the eruption of Mt. Pinatubo is also seen. Including the interannual variability in temperature and transport (red line) allows the model to qualitatively resolve some of the yearly and QBO-like variations in the data, although the model tends to underestimate the observed amplitudes.

[58] At midlatitudes, the effects of the halogen and aerosol loading are more significant in the SH relative to the NH in the model (blue dotted line), and this is likely related to the hemispheric asymmetry in late winter-spring polar ozone loss [e.g., *WMO*, 2003, 2007]. From 1979 to the late 1990s, the halogen-induced ozone decreases were 11 DU (~3%) at NH midlatitudes and 26 DU (~8.5%) at SH midlatitudes. The simulated dynamical changes including the QBO-like variability tend to be a bit better resolved in the NH, which is likely due to the denser radiosonde coverage contained in the meteorological analyses in the NH. Although the model does not capture all of the observed shorter term (~2–3 years) variability in a quantitative sense, there is reasonable qualitative agreement at all latitudes, as noted in Figure 8. Although underestimated compared with the data, the full model A simulation (red line) qualitatively reveals a drop during 1985 in the SH, suggesting that this decrease is at least partly dynamically driven. This was also noted by *Chipperfield* [2003] using the three-dimensional SLIMCAT CTM driven by the ECMWF analyses.

[59] At the equator the halogen effect is small as expected, with a decrease of 3 DU (~1%) from 1979 to 2000. The influence of the aerosol surface area density is also mostly small, except for the ~2–3 DU decrease during 1992–1993 associated with the Pinatubo eruption. The solar cycle effect contributes roughly 4 DU (~1.5%) from solar maximum to solar minimum, consistent with previous studies [e.g., *Jackman et al.*, 1996; *Geller and Smyshlyaev*, 2002]. However, the QBO is by far the largest source of variability at the equator. As illustrated in Figure 10, model A captures the phase of the observations quite well, although the simulated amplitude tends to be underestimated during certain years (1984, 1990, and 1992).

6.2. Polar Ozone Time Series

[60] While long-term time series comparisons such as in Figure 12 are not possible at polar latitudes because of the lack of data during polar night, here we present model-data comparisons for the specific spring-summer seasons. The spring months are typically characterized by large interannual fluctuations in both the northern and southern polar regions. Figure 13 (top panel) shows the October monthly and zonal mean total ozone for the SH polar region (60°S–80°S average) from the TOMS/SBUV data for 1979–2004 (black asterisk-solid line). The well-known decrease in Antarctic ozone during the 1980s and 1990s due to the increased halogen loading is seen. The chemical destruction of ozone within the Antarctic vortex occurs regularly each year so that interannual variability is not generally large during September–October. Exceptions to this occur during 1987–1988 and 2000–2004 when interannual fluctuations are notably large. Also shown are results from model A (solid red line), which uses the NCEP-derived transport, and model E (solid green line), which is model A without the interannual dynamical variability.

[61] Although the two-dimensional model formulation is not expected to adequately simulate the zonally asymmetric and highly nonlinear chemistry of the Antarctic lower stratosphere during winter/early spring, incorporation of the longitudinal temperature probability distributions and the insolation correction in the model chemistry partially accounts for these processes (see section 2.3). For example, the model simulates a large area of type I and type II PSCs

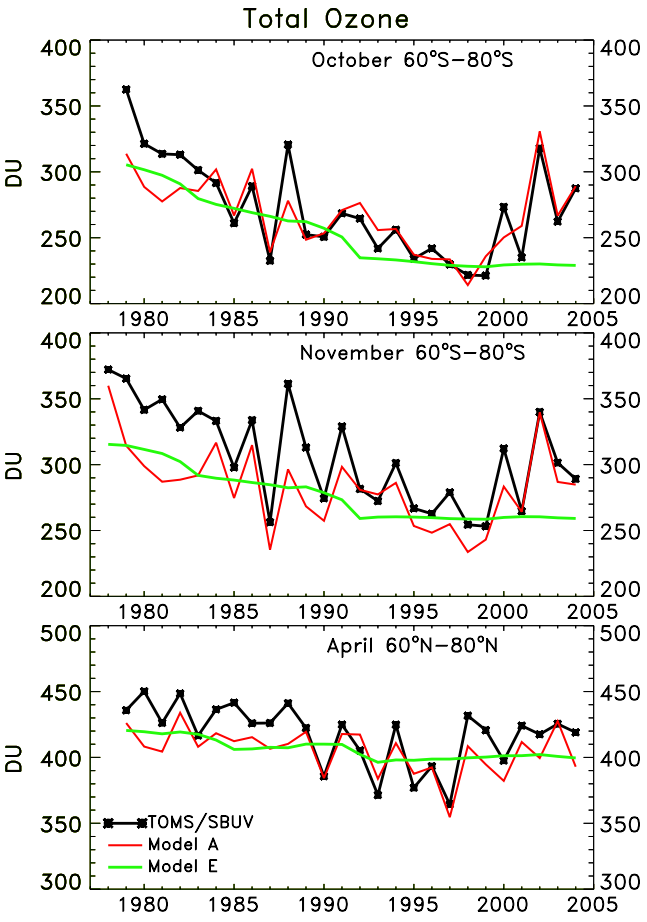

Figure 13. Springtime monthly and area-weighted average polar total column ozone for 1978–2004 for the months and latitude zones indicated. Shown are the TOMS/SBUV merged ozone data set (black line-asterisks), and model simulations A (red line) and E (green line) listed in Table 1.

throughout the Antarctic winter [see also *Considine et al.*, 1994], leading to significant denitrification and heterogeneous conversion of $ClONO_2$ and HCl to the radical chlorine species. As seen in Figure 6 during September–October, the model is in reasonable agreement with the observed ozone equatorward of ~80°S. However, deep within the vortex at 80°S–90°S, the model underestimates the depth of ozone hole by as much as 50–70 DU. This is likely due to the model, even with the insolation correction, underestimating the amount of sunlight that air parcels experience poleward of ~80° during September–October. This leads to an underestimation in the amount of chlorine activation and catalytic ozone loss in the simulation. This systematic model bias disappears equatorward of ~80°S where there is a greater amount of sunlight during September–October. We note that, given the small areal coverage poleward of 80°S, this model ozone surplus does not appreciably affect the simulated ozone later in the spring, via a dilution effect, following the breakup of the vortex and subsequent mixing of ozone-poor air to lower altitudes and lower latitudes.

[62] As seen in Figure 13, model E (without the interannual variability) during October at 60°S–80°S reveals a decline of 77 DU from 1979 to 1998 primarily due to the halogen loading. Smaller declines due to the aerosol enhancements are seen in 1983 and 1992 following the eruptions of El Chichon and Pinatubo. The solar cycle variations of 4–5 DU from solar minimum to solar maximum are comparatively quite small in model E. Superimposed on these processes are the year-to-year dynamical variations seen in the data which are qualitatively captured fairly well in model A, although the anomalously high ozone in 1988 and 2000 is underestimated in the model. The absolute values of ozone are also mostly well simulated in model A, although they are somewhat underestimated prior to 1983. Given that model E is relatively flat after 1998, comparison of model A and model E suggests that the increase in the observed October SH polar ozone between 1998 and 2004 is caused by interannual dynamical variability rather than decreases in the atmospheric halogen loading.

[63] By November, as polar temperatures have warmed above the threshold for formation of type I and II PSCs [e.g., *WMO*, 2003], the Antarctic heterogeneous chemical ozone loss has mostly shut off, and interannual fluctuations are typically larger than occur earlier in the spring (Figure 13, middle panel). Although model A tends to underestimate the observed ozone by an average of ~20 DU in November (see also Figure 6), the observed year-to-year variations are again resolved quite well in the simulation. While the decrease in model E is ~55 DU from 1978 to 1992 (~4 DU/year) and is mainly flat after 1992, the interannual dynamical changes are significantly bigger. This is particularly true during 1986–1992 and 1999–2003, in which the year-to-year changes seen in the data are as much as 50–100 DU, with model A qualitatively capturing much of these fluctuations. The very high ozone amounts occurring during the highly perturbed spring seasons of 1988 and 2002 are particularly noticeable.

[64] In the NH spring (Figure 13, bottom panel), the simulated decrease in model E is 25 DU from 1979 to 1993, which is significantly smaller than simulated in the SH because of the greatly reduced ozone loss caused by heterogeneous processes in the NH. These primarily halogen-induced changes are significantly smaller than the observed year-to-year dynamically induced fluctuations in the NH, which can be as large as 50–70 DU, for example during 1992–1998. This point was also discussed in the three-dimensional CTM study of *Chipperfield and Jones* [1999]. Here again model A qualitatively captures much of this observed NH dynamical variability.

[65] Although our current two-dimensional model includes the longitudinal corrections discussed in section 2.3, the simulations cannot resolve much of the large zonal asymmetry characteristic of the polar regions during the SH springtime and the NH winter-spring. However, in terms of the zonal mean ozone, the primary drivers of the polar springtime variability seen in Figure 13 are the interannual changes in stratospheric planetary wave activity and the resulting residual circulation and temperature changes [e.g., *Newman et al.*, 2001], and these processes appear to be well resolved in the model. Years with larger planetary wave activity, primarily during mid–late winter, generate a stronger residual circulation and a greater transport of ozone into the polar regions (for example, 1988, 2000, and 2002 in the SH; 1998 and 1999 in the NH). Years with enhanced wave activity will also result in warmer polar temperatures and, in the SH, an earlier cessation of the ozone loss due to heterogeneous chemical processes (for example, 1988).

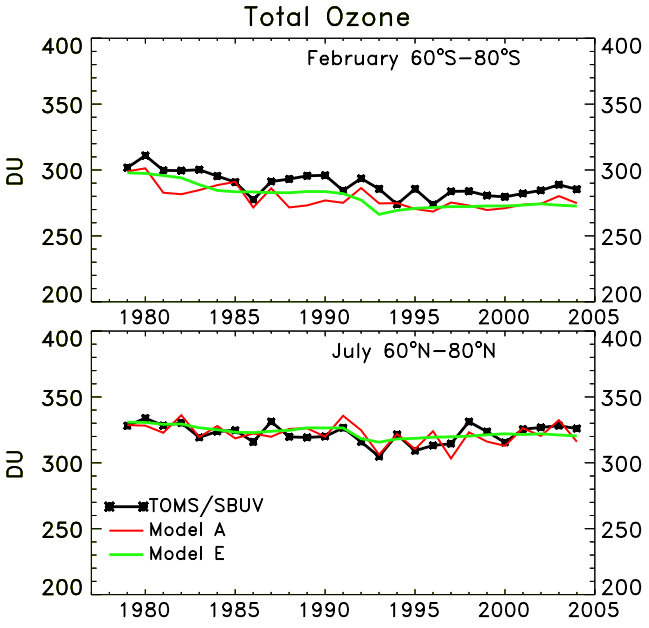

Figure 14. Summertime monthly and area-weighted average polar total column ozone for 1979–2004 for the months and latitude zones indicated. Shown are the TOMS/SBUV merged ozone data set (black line-asterisks), and model simulations A (red line) and E (green line) listed in Table 1.

Conversely, low-wave-activity years result in lower ozone concentrations because of the weaker transport of ozone into the polar region and longer duration heterogeneous processing due to the colder polar temperatures. While this latter process occurs primarily in the SH, it is also simulated in our model in the NH polar spring during very cold years such as 1996 and 1997.

[66] For comparison, we also show analogous time series for the summer months in Figure 14. Here much smaller variability is observed in both hemispheres because of the much weaker planetary wave activity relative to winter-spring. The interannual changes are at most 10–20 DU in each hemisphere. These are comparable to the halogen and aerosol-induced changes over the 1979–2004 time period, which are ~30 DU in the SH summer and ~15 DU in the NH summer. Model A qualitatively resolves many of the weak year-to-year fluctuations observed in both hemispheres. While the absolute values of both models are quite close to the data in the NH, the models in the SH underestimate the summertime observations by an average of 10 DU over the time period.

6.3. Halogen Trend

[67] Figure 15 shows latitudinal profiles of the trend in total ozone for 1979–1996 derived from the regression analysis of the observed and simulated time series. As discussed in *Stolarski et al.* [2006] (see also section 3), this trend is obtained from the regression analysis by fitting a term for the entire time series, 1979–2004, that represents the effective halogen loading of the stratosphere. This term is linear for 1979–1996 and accounts for the leveling off of stratospheric halogen loading after 1996. The resulting trends for the 1979–1996 time period, expressed in DU/decade, are shown in Figure 15 along with the 2σ uncertainty bars. The derived trend from model E (green line) reveals latitudinal variations that are qualitatively similar to the trend derived from observations, with moderate negative values at NH midlatitudes and larger negative values at SH midlatitudes which are greater than the 2σ uncertainty of the observations. The derived result for model E also shows a small negative trend in the tropics, while the observations show a near-zero trend. These results of model E are generally similar to those reported in the three-dimensional CTM study of Stolarski et al. We note also that the results for model E in Figure 15 are nearly identical to those derived from model C (halogen loading only), illustrating the very small impact that the aerosol loading and solar cycle variations have on the trend derived from the simulations.

[68] Figure 15 also shows the derived trend for 1979–1996 from a simulation in which only the interannual variations in transport and temperature are included (model G, blue dashed line). While there is no explicit halogen loading in this simulation, it is possible that the halogen loading and subsequent ozone changes in the real atmosphere may induce dynamical changes that would be reflected in the meteorological data and therefore in model G. A significantly positive trend is obtained at high SH latitudes in this simulation. However, at most latitudes, model G reveals a derived trend which is mostly small and not outside the 2σ uncertainties. To examine this point further, we reran the regression by fitting a standard linear term to the 1979–2004 time series of model G (no halogen term was used). Such a fit would be appropriate if a long-term trend in dynamics is due to, for example, increasing green house gas emissions. However, this derived trend was nearly identical to that derived from the halogen proxy shown in Figure 15.

[69] The 1979–1996 trend for the full model A, derived using the halogen proxy in the regression (Figure 15,

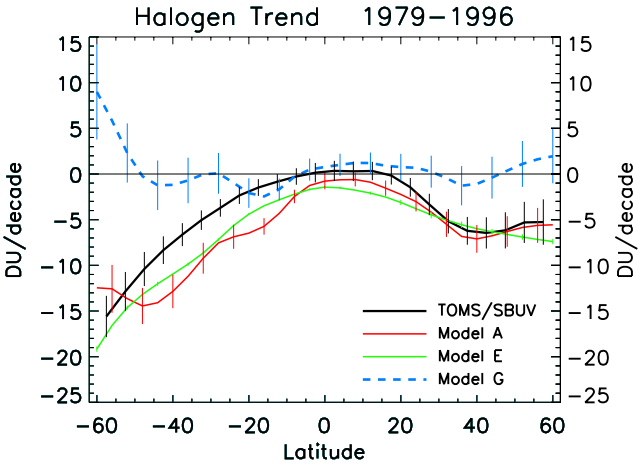

Figure 15. Latitude profiles of the annually averaged trend in total ozone and 2σ uncertainties, derived from the regression analysis. Results are shown for the TOMS/SBUV merged ozone data set (black line), model simulation A (red solid line), model simulation E (green solid line), and model simulation G (blue dashed line). The trends are for the time period 1979–1996, calculated using data/output for 1979–2004 and the effective halogen loading proxy described in the text.

red line), reflects the latitudinal variations seen in model G. Inclusion of the interannual dynamical variability in model A results in a derived trend that is closer to the observations in the tropics and NH midlatitudes compared with model E. The trend derived from the data in the tropics is near zero, and the maximum negative trend in the NH observations occurs near 40°N, not at high latitudes. These features are reproduced in the trend derived from model A, but not model E, and suggest the influence of interannual variability on the details of the observationally derived trend. However, overall the trend derived from model A is similar in magnitude to that of model E at most latitudes. This suggests that halogen loading is the dominant mechanism responsible for the data-derived trend at midlatitudes of both hemispheres in Figure 15.

6.4. Solar Cycle Effects

[70] In this section we focus on the effects of the 11-year solar cycle variation in UV flux. Figure 16 (top panel) shows latitudinal profiles of the solar cycle response derived from the regression analysis of the observed time series for 1979–2004 (black line). These results are consistent with previous work [e.g., *WMO*, 2003; *Stolarski et al.*, 2006]. Values are greater than the 2σ uncertainty for 40°S–40°N and range from 4 to 6 DU per 100 units of F10.7. This corresponds to ~5–8 DU, or ~2–3%, from solar maximum to solar minimum. The solar cycle response from model simulation A (red line) shows a roughly consistent latitudinal structure. Although the modeled magnitudes at low latitudes are smaller than seen in the data presented here, they are generally in line with the solar cycle response derived from multidecadal ground-based and SBUV/SBUV-2 data sets, which have large uncertainties [*WMO*, 2003].

[71] To examine the solar cycle effects on the simulations in more detail, we include additional model results in the bottom panel of Figure 16. Previous modeling studies have examined the photochemical effect due to the 11-year solar cycle as changes in UV flux directly modify the production rate of ozone giving a broad latitudinal response [e.g., *Huang and Brasseur*, 1993; *Fleming et al.*, 1995; *Lee and Smith*, 2003]. This effect is captured in model simulation F (Table 1) in which the solar cycle UV variations are the only perturbation input into the model. The resulting solar cycle response from the regression analysis is shown in the bottom panel of Figure 16 (dotted green line) and reveals a roughly constant latitudinal response of 3 DU per 100 units F10.7 with very small 2σ uncertainty. This corresponds to a ~1.5% change from solar maximum to solar minimum.

[72] In addition to the direct photochemical effect, the possibility of a dynamical feedback component of the solar cycle response, in which the UV variations impact the temperature, circulation, and planetary wave propagation characteristics of the stratosphere, has been a topic of ongoing research [e.g., *Hood et al.*, 1993; *Kodera and Kuroda*, 2002; *Salby and Callaghan*, 2004a]. Such a response could be present in the meteorological data [e.g., *Salby and Callaghan*, 2004a] from which we derive our interannually varying model transport. To investigate this effect on the total ozone simulations, we utilize model G in which only the interannual meteorological variability (from NCEP) is included. The solar cycle response derived

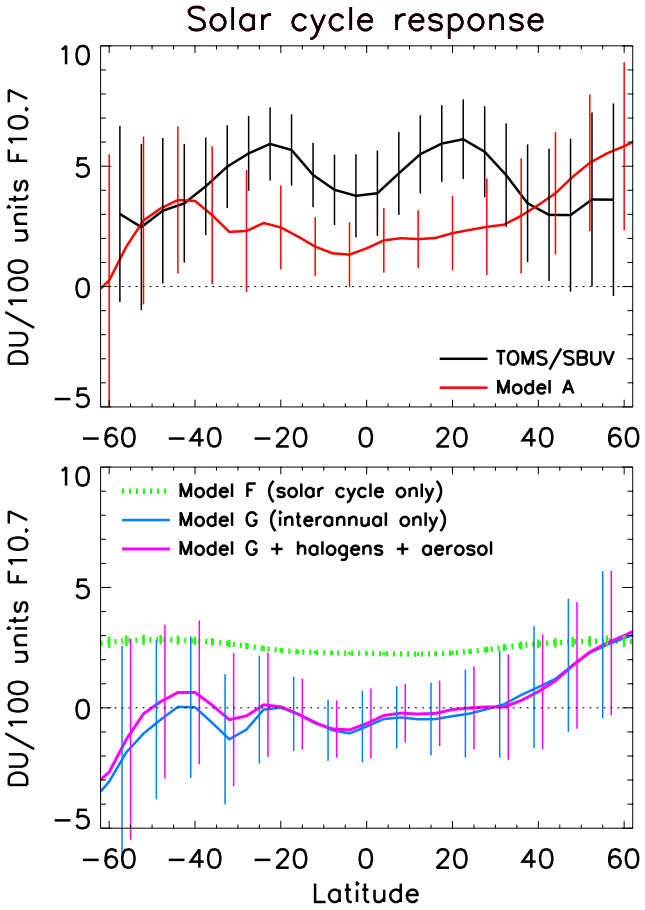

Figure 16. Latitude profiles of the annually averaged solar cycle response in total ozone (in DU per 100 units F10.7-cm flux) for 1979–2004 as derived from the regression analysis. Also shown are the 2σ uncertainty bars. Top panel shows results for the TOMS/SBUV merged ozone data set (black line) and model simulation A (red line). Bottom panel shows results from model simulation F (containing only the solar cycle UV flux variations, dotted green line), model simulation G (containing only the interannual dynamical variations, blue line), and model simulation G with the time-dependent halogen and aerosol loading included (purple line).

from the regression analysis of this simulation is depicted by the blue line in the bottom panel of Figure 16. However, the response is very small at most latitudes, with large uncertainty due to the large interannual dynamical variability, making it far from statistically significant at 2σ. The response is largest just off the plot at 65°S and 65°N (−3 DU and +3 DU per 100 units F10.7, respectively). But these again are not statistically detectable given the very large interannual variability inherent at high latitudes.

[73] Previous studies have examined the potential difficulties with using a limited duration time series to extract a solar cycle signal via multiple regression. For example, *Lee and Smith* [2003] discussed how variability from other processes such as the QBO and the El Chichon and Pinatubo volcanic eruptions may not completely be separated from the solar cycle signal in profile ozone. The

meteorological data used in model G contain effects of the major volcanic eruptions, most notably the lower stratospheric warming during 1982–1983 and late 1991–1992 [e.g., *WMO*, 2003, see Figures 4–22]. We attempt to estimate how these volcanic signals may contaminate the solar cycle signal obtained from the regression for model G. To do this, we include the time-dependent halogen and aerosol loading in model G (i.e., model A without the solar cycle), thereby significantly perturbing the simulated column ozone following the El Chichon and Pinatubo eruptions. However, the derived solar cycle response in Figure 16 (bottom panel, purple line) is virtually the same as in model G alone (bottom panel, blue line). This suggests that the absence of a statistically detectable solar signal in total ozone in model G is likely not caused by interference in the regression from volcanic signals contained in the meteorological data.

[74] The solar cycle response derived from model simulation A (top panel, red line) therefore is driven primarily by the direct photochemical effect (bottom panel, green dashed line), with the latitudinal variations caused by the small and not statistically significant interannual variability effect (bottom panel, blue line). Note that the response in model A is nearly identical to the sum of the responses from the solar-cycle-only simulation (F) and the interannual-variability-only simulation (G).

6.5. Effects of the Pinatubo Aerosol

[75] We now focus on the 1991–1995 time period, in which the stratospheric aerosol loading increased dramatically during the few years following the eruption of Mt. Pinatubo. On the basis of the input-observed aerosol distribution, chemically induced ozone loss would be expected in both hemispheres following the eruption. However, such an effect, while present in the NH, appears to be absent or is greatly mitigated in the total ozone data in the SH [e.g., *WMO*, 2003]. The recent study of *Stolarski et al.* [2006] speculated that this may be due to interannual dynamical variability which masks the Pinatubo chemical effect in the SH.

[76] To illustrate this point, Figure 17 shows latitudinal profiles of the maximum annually averaged response to the Pinatubo aerosols derived from the regression analysis. The fit to the observational time series (black line) shows a large effect poleward of 35°N, maximizing at −20 DU near 60°N. At high SH latitudes, the effect is smaller (−5 to −7 DU at 55°S–60°S) and is only marginally detectable at 2σ. The observational response in the tropics and most of the SH is small (<−5 DU) and is statistically significant at 2σ only at lower latitudes. At 30°S–30°N, the fit to model A time series (red solid line) is generally consistent with the data within the uncertainty bars. However, model A significantly underestimates the observed signal in the NH poleward of 40°N. The response from model B (using the ERA-40 meteorology, red dashed-dotted line) is generally similar to model A, except in the NH poleward of 35°N where it is larger and is closer to the observed response (the 2σ uncertainty bars for model B are not plotted for visual clarity but have magnitudes similar to model A). We note that the derived Pinatubo response from model A is nearly identical to that of the same model simulation without the solar cycle UV variations, suggesting very little interference between the two signals in the multiple regression of the observed time series.

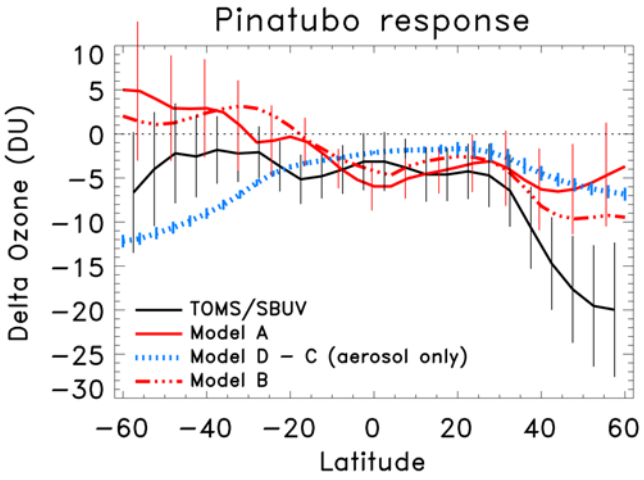

Figure 17. Latitude profiles of the maximum annually averaged Pinatubo response in total ozone and 2σ uncertainties, derived from the regression analysis. Results are shown for the TOMS/SBUV merged ozone data set (black line), model simulation A (red solid line), model simulation B (red dashed-dotted line), and simulation D minus simulation C which gives the aerosol-only chemical effect (blue dotted line). For visual clarity, the 2σ uncertainties for model B are not plotted but are similar to model A.

[77] Figure 17 also shows the Pinatubo fit to a simulated time series in which model C has been subtracted from model D (blue dotted line), which isolates the effects of the aerosol perturbation on the model chemistry. Consistent with the aerosol distribution input into the model, this "aerosol-only" simulation exhibits a SH response that is significantly larger than seen in either the observations or models A and B. A similar result was obtained in the three-dimensional CTM study of *Stolarski et al.* [2006]. The response in the tropics is similar among all three models and the observations. In the NH, the aerosol-only simulation significantly underestimates the observed fit and tends to be smaller than the response of model A and especially of model B. These results suggest that interannual variability masks the Pinatubo aerosol chemical effect in the SH, but enhances the effect in the NH.

[78] To examine this point further, Figure 18 shows a close-up for 1991–1995 of the observed midlatitude deseasonalized total ozone time series (black line-asterisks) and model simulation A (red line), as in Figure 12. We also show the aerosol-only simulation (model D minus model C, blue dotted line) and model G (interannual variability only, green line). As in Figure 17, the aerosol-only effect is largest in the SH, maximizing at −13 DU during late 1992, with a smaller −7 DU effect in the NH during early 1993. The associated NO_2 field from simulation A (not shown) shows sharp reductions starting in late 1991 with corresponding increases in HNO_3 associated with the heterogeneous conversion on sulfate aerosols of N_2O_5 to the reservoir HNO_3. These NO_2 reductions are larger in the SH and are consistent with measurements taken at Lauder, New Zealand (45°S) and Jungfraujoch, Switzerland (46°N) [see

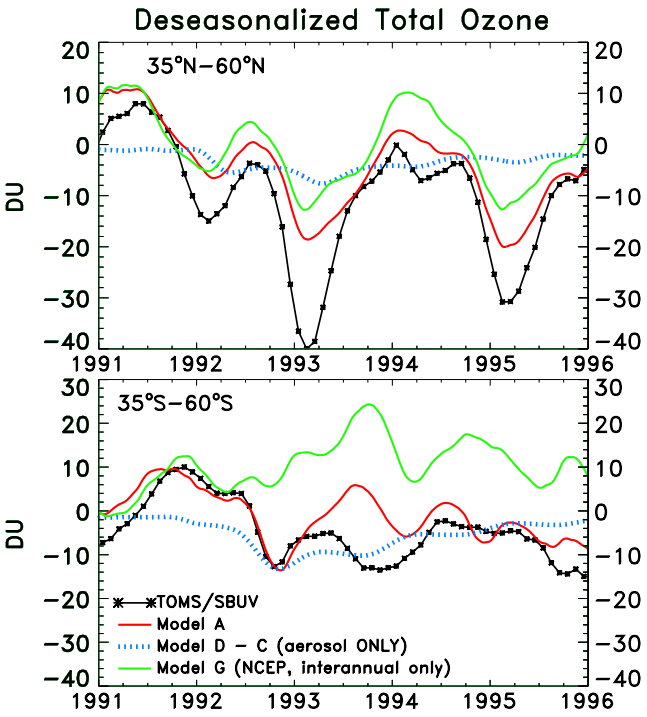

Figure 18. Time series of deseasonalized total ozone (DU) for 1991–1995 from the TOMS/SBUV merged ozone data set, and model simulations using the NCEP meteorology as indicated. See text and Table 1 for details.

De Maziere et al., 1998; *Liley et al.*, 2000; *WMO*, 2003]. Model A also shows large increases in ClO as the heterogeneous conversion of N_2O_5 and $ClONO_2$ allows more chlorine to exist in radical form [e.g., *Tie et al.*, 1994], leading to enhanced ozone loss which is greater in the SH.

[79] In the NH, the modeled interannual variability seen in model G acts to decrease ozone during the winter months, thereby reinforcing the aerosol effect during early 1992 and especially during early 1993. This is more clearly seen in Figure 19, which shows the analogous set of model simulations using the ERA-40 meteorology (simulations B, D minus C, and H). As noted previously, the ERA-40-based interannual variability is qualitatively consistent, albeit with greater magnitudes, compared with the NCEP-based interannual variability in both hemispheres. These simulations suggest that the large NH ozone drop during early 1993 seen in the data is due in large part to the interannual dynamical variability, with the chemical loss due to enhanced aerosols contributing a significantly smaller effect. This is consistent with the three-dimensional CTM studies of *Hadjinicolaou et al.* [1997] and *Chipperfield* [1999] who concluded that interannual dynamical variability contributed to the low observed ozone at NH midlatitudes during 1992–1993. It is also likely that some of the modeled interannual variability derived from the meteorological analyses seen in Figures 18 and 19 is due to the Pinatubo aerosol perturbation, which induced heating rate and stratospheric circulation changes in the years following the eruption [e.g., *Tie et al.*, 1994; *Kinnison et al.*, 1994; *Rosenfield et al.*, 1997; *Kirchner et al.*, 1999; *Al-Saadi et al.*, 2001; *WMO*, 2003].

[80] In the SH, the interannual-variability-only simulations (G and H) reveal relatively small positive ozone anomalies during most of 1992 and suggest that the aerosol chemical effect is primarily responsible for much of the observed ozone decreases during mid-late 1992. However, during 1993, there are larger positive ozone changes caused by the interannual variability that tend to mitigate or even cancel the aerosol-induced chemical ozone reductions in the model. These model results are qualitatively consistent between the two sets of meteorological analyses and suggest that the small annually averaged SH Pinatubo response in the data in Figure 17 is at least partly caused by interannual variability which masks the chemical effect.

7. Summary and Conclusions

[81] In this paper, we describe an updated version of our GSFC two-dimensional model and provide a general model evaluation by comparing simulated and observed climatological long-lived tracers (age of air, H_2O, and CH_4), chlorine species (HCl and $ClONO_2$), and vertical profile and total column ozone. These comparisons reveal good qualitative model-data agreement, illustrating that the simulations can resolve many of the transport-sensitive features seen in the observations in the lower stratosphere.

[82] We then use the model to study the effects of interannual dynamical variability on total ozone simulations for 1979–2004. Long-term meteorological data from the NCEP-NCAR reanalysis-2 project and the ECMWF ERA-40 are used to construct the yearly transport and temperature fields for use in the simulations. Use of statistical regression analysis allows us to isolate signals associated with the

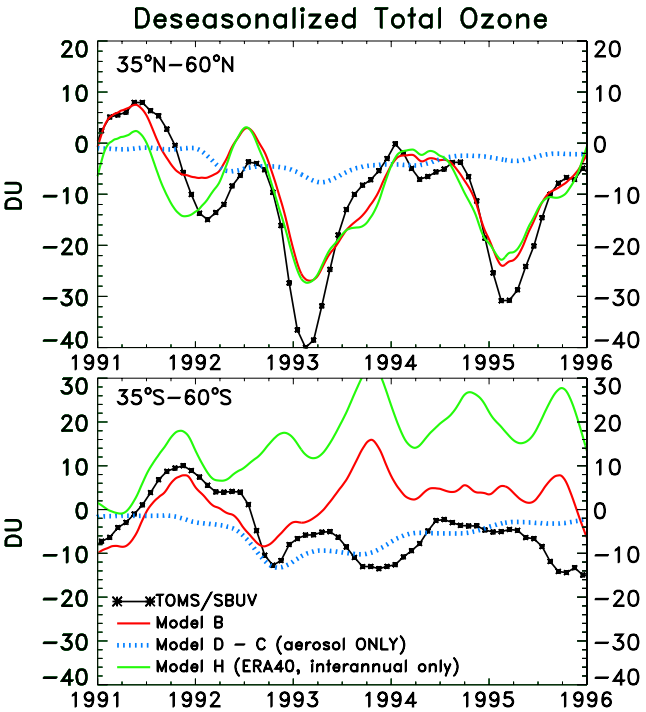

Figure 19. Time series of deseasonalized total ozone (DU) for 1991–1995 from the TOMS/SBUV merged ozone data set, and model simulations using the ERA-40 meteorology as indicated. See text and Table 1 for details.

QBO, the 11-year solar cycle, the El Chichon and Pinatubo volcanic eruptions, and the halogen-induced trend. The residual circulation framework of the two-dimensional model qualitatively simulates much of the seasonal and interannual variability observed in long-term satellite-based total ozone data in the tropics and extratropics. The observed year-to-year variations are dominated by QBO-like fluctuations on a global scale. The model resolves these features fairly well, including amplitude maxima in the tropics which are opposite in phase with the midlatitude maxima in both hemispheres and amplitude minima in the subtropics. The observed seasonality of the QBO signal is also captured globally using this empirically based model transport.

[83] A series of model experiments reveals the relative roles that the halogen and volcanic aerosol changes, the 11-year solar cycle variations, and interannual dynamical variability have on the long-term total ozone distributions. These simulations illustrate the large impact of interannual variability in driving the year-to-year total ozone changes on a global basis. The halogen and aerosol loading and solar cycle variations are significant at midlatitudes of both hemispheres. However, at the equator, the large fluctuations due to the QBO have by far the largest impact on total ozone.

[84] In the polar region (60°–80°) of both hemispheres during spring, the model simulates the observed interannual variations in total ozone quite well. Much of this variability is due to the year-to-year changes in planetary wave activity and the related changes in the strength of the residual circulation which is well resolved by the model transport. During the polar spring in both hemispheres, this yearly variability is significantly larger than the ozone changes caused by the halogen and aerosol loading. Polar ozone fluctuations due to the 11-year solar cycle are very small compared with the dynamical variations. During the polar summer, interannual changes are considerably smaller relative to the springtime and are comparable to the halogen- and aerosol-induced changes.

[85] As simulated using both sets of meteorological data, the model reveals that, at Northern midlatitudes, interannual dynamical variability tends to reinforce the chemical ozone depletion caused by the enhanced aerosol loading following the Pinatubo eruption. However, at Southern midlatitudes, the interannual variability masks the aerosol-induced chemical effect.

[86] Model results also show that the simulated solar cycle response in total ozone of 2–4 DU per 100 units of F10.7-cm flux is generally consistent with the observations. Most of this response is due to the direct photochemical effect, with any indirect dynamical effect found to be statistically undetectable at the 2σ level.

[87] The simulation incorporating only the interannual dynamical variability yielded a derived total ozone trend for 1979–1996 that is statistically significant (positive) only at 50°S–60°S. Outside of this region (40°S–60°N), the derived trend is small and is statistically undetectable at the 2σ level. The derived 1979–1996 trend from the full model is quite close to that calculated from the observations in the tropics and NH. At SH midlatitudes, the model-derived trend for 1979–1996 appears to be more sensitive to halogen loading than the trend derived from the data. Taken together, the simulations suggest that the total ozone trend for 1979–1996 calculated from the observations at midlatitudes of both hemispheres is dominated by the trend due to halogen loading, with any dynamically induced trend playing a secondary role.

[88] **Acknowledgments.** We thank Jerry Ziemke, Rich Stolarski, and Stacey Frith for the use of their statistical regression routines and for help with the analysis. We are also grateful to Joan Rosenfield for supplying her updated radiation code, Dong Wu for supplying the UARS/MLS mesospheric temperature data, Gordon Labow for supplying the ozone profile climatology, Darryn Waugh for supplying the age of air observations, David Considine for supplying the stratospheric aerosol data set, and Hans Schneider for supplying the routines to perform the off-diagonal eddy diffusion calculation. We thank the NASA Atmospheric Chemistry Modeling and Analysis Program for support of this project. We also thank three anonymous reviewers for their helpful comments.

References

Al-Saadi, J. A., R. B. Pierce, T. D. Fairlie, M. M. Kleb, R. S. Eckman, W. L. Grose, M. Natarajan, and J. R. Olson (2001), Response of middle atmosphere chemistry and dynamics to volcanically elevated sulfate aerosol: Three-dimensional coupled model simulations, *J. Geophys. Res.*, *106*, 27,255–27,275.

Andrews, D. G., J. R. Holton, and C. B. Leovy (1987), *Middle Atmosphere Dynamics*, 498 pp., Elsevier, New York.

Baldwin, M. P., et al. (2001), The quasi-biennial oscillation, *Rev. Geophys.*, *39*, 179–229.

Callis, L. B., M. Natarajan, J. D. Lambeth, and R. E. Boughner (1997), On the origin of midlatitude ozone changes: Data analysis and simulations for 1979–1993, *J. Geophys. Res.*, *102*, 1215–1228.

Chipperfield, M. P. (1999), Multiannual simulations with a three-dimensional chemical transport model, *J. Geophys. Res.*, *104*, 1781–1805.

Chipperfield, M. P. (2003), A three-dimensional model study of long-term mid-high latitude lower stratosphere ozone changes, *Atmos. Chem. Phys.*, *3*, 1253–1265.

Chipperfield, M. P., and R. L. Jones (1999), Relative influences of atmospheric chemistry and transport on Arctic ozone trends, *Nature*, *400*, 551–554.

Chou, M.-D., and M. J. Suarez (1999), A solar radiation parameterization for atmospheric studies, in *NASA Tech. Memo.*, *NASA/TM-1999-104606*, vol. 15, 40 pp.

Chou, M.-D., M. J. Suarez, X.-Z. Liang, and M. M.-H. Yan (2001), A thermal infrared radiation parameterization for atmospheric studies, in *NASA Tech. Memo.*, *NASA/TM-2001-104606*, vol. 19, 56 pp.

Considine, D. B., A. R. Douglass, and C. H. Jackman (1994), Effects of a polar stratospheric cloud parameterization on ozone depletion due to stratospheric aircraft in a two-dimensional model, *J. Geophys. Res.*, *99*, 18,879–18,894.

De Maziere, M., M. Van Roozendael, C. Herman, P. C. Simon, P. Demoulin, G. Roland, and R. Zander (1998), Quantitative evaluation of post-Pinatubo NO_2 reduction and recovery, based on 10 years of FTIR and UV-visible spectroscopic measurements at the Jungfraujoch, *J. Geophys. Res.*, *103*, 10,849–10,858.

Douglass, A. R., C. H. Jackman, and R. S. Stolarski (1989), Comparison of model results transporting the odd nitrogen family with results transporting separate odd nitrogen species, *J. Geophys. Res.*, *94*, 9862–9872.

Dunkerton, T. J. (1997), The role of gravity waves in the quasi-biennial oscillation, *J. Geophys. Res.*, *102*, 26,053–26,076.

Fleming, E. L., S. Chandra, C. H. Jackman, D. B. Considine, and A. R. Douglass (1995), The middle atmospheric response to short and long term solar UV variations: analysis of observations and 2D model results, *J. Atmos. Terr. Phys.*, *57*, 333–365.

Fleming, E. L., C. H. Jackman, R. S. Stolarski, and D. B. Considine (1999), Simulation of stratospheric tracers using an improved empirically based two-dimensional model transport formulation, *J. Geophys. Res.*, *104*, 23,911–23,934.

Fleming, E. L., C. H. Jackman, D. B. Considine, and R. S. Stolarski (2001), Sensitivity of tracers and a stratospheric aircraft perturbation to two-dimensional model transport variations, *J. Geophys. Res.*, *106*, 14,245–14,263.

Fleming, E. L., C. H. Jackman, J. E. Rosenfield, and D. B. Considine (2002), Two-dimensional model simulations of the QBO in ozone and tracers in the tropical stratosphere, *J. Geophys. Res.*, *107*(D23), 4665, doi:10.1029/2001JD001146.

Froidevaux, L., et al. (2006), Early validation analyses of atmospheric profiles from EOS MLS on the Aura satellite, *IEEE Trans. Geosci. Remote Sens.*, *44*(5), 1106–1121.

Fusco, A. C., and M. L. Salby (1999), Interannual variations of total ozone and their relationship to variations of planetary wave activity, *J. Clim.*, *12*, 1619–1629.

Garcia, R. R., and S. Solomon (1983), A numerical model of the zonally averaged dynamical and chemical structure of the middle atmosphere, *J. Geophys. Res.*, *88*, 1379–1400.

Geller, M. A., and S. P. Smyshlyaev (2002), A model study of total ozone evolution 1979–2000—the role of individual natural and anthropogenic effects, *Geophys. Res. Lett.*, *29*(22), 2048, doi:10.1029/2002GL015689.

Gelman, M. E., A. J. Miller, K. W. Jihnson, and R. N. Nagatani (1986), Detection of long term trends in global stratospheric temperature from NMC analyses derived from NOAA satellite data, *Adv. Space Res.*, *6*, 17–26.

Gray, L. J., and J. A. Pyle (1989), A two-dimensional model of the quasi-biennial oscillation of ozone, *J. Atmos. Sci.*, *46*, 203–220.

Gray, L. J., and S. Ruth (1993), The modeled latitudinal distribution of the ozone quasi-biennial oscillation using observed equatorial winds, *J. Atmos. Sci.*, *50*, 1033–1046.

Hadjinicolaou, P., J. A. Pyle, M. P. Chipperfield, and J. A. Kettleborough (1997), Effect of interannual meteorological variability on midlatitude O_3, *Geophys. Res. Lett.*, *24*, 2993–2996.

Hadjinicolaou, P., A. Jrrar, J. A. Pyle, and L. Bishop (2002), The dynamically driven long-term trend in stratospheric ozone over northern middle latitudes, *Q. J. R. Meteorol. Soc.*, *128*, 1393–1412.

Hadjinicolaou, P., J. A. Pyle, and N. R. P. Harris (2005), The recent turnaround in stratospheric ozone over northern middle latitudes: A dynamical modeling perspective, *Geophys. Res. Lett.*, *32*, L12821, doi:10.1029/2005GL022476.

Hall, T. M., and R. A. Plumb (1994), Age as a diagnostic of stratospheric transport, *J. Geophys. Res.*, *99*, 1059–1070.

Hall, T. M., and D. W. Waugh (1997), Tracer transport in the tropical stratosphere due to vertical diffusion and horizontal mixing, *Geophys. Res. Lett.*, *24*, 1383–1386.

Hall, T. M., and D. W. Waugh (1998), Influence of nonlocal chemistry on tracer distributions: Inferring the mean age of air from SF_6, *J. Geophys. Res.*, *103*, 13,327–13,336.

Hall, T. M., D. W. Waugh, K. A. Boering, and R. A. Plumb (1999), Evaluation of transport in stratospheric models, *J. Geophys. Res.*, *104*, 18,815–18,839.

Hasebe, F. (1994), Quasi-biennial oscillations of ozone and diabatic circulation in the equatorial stratosphere, *J. Atmos. Sci.*, *51*, 729–745.

Hollandsworth, S. M., K. P. Bowman, and R. D. McPeters (1995), Observational study of the quasi-biennial oscillation in ozone, *J. Geophys. Res.*, *100*, 7347–7361.

Holton, J. R., and X. Zhu (1984), A further study of gravity wave induced drag and diffusion in the mesosphere, *J. Atmos. Sci.*, *41*, 2653–2662.

Holton, J. R. (1986), Meridional distribution of stratospheric trace constituents, *J. Atmos. Sci.*, *43*, 1238–1242.

Hood, L. L., J. L. Jirikowic, and J. P. McCormack (1993), Quasi-decadal variability of the stratosphere: Influence of long-term solar ultraviolet variations, *J. Atmos. Sci.*, *50*, 3941–3958.

Hood, L. L., J. P. McCormack, and K. Labitzke (1997), An investigation of dynamical contributions to midlatitude ozone trends in winter, *J. Geophys. Res.*, *102*, 13,079–13,093.

Hood, L. L., B. Soukharev, M. Fromm, and J. P. McCormack (2001), Origin of extreme ozone minima at middle to high northern midlatitudes, *J. Geophys. Res.*, *106*, 20,925–20,940.

Hood, L. L., and B. Soukharev (2003), Quasi-decadal variability of the tropical lower stratosphere: The role of extratropical wave forcing, *J. Atmos. Sci.*, *60*, 2389–2403.

Hood, L. L., and B. Soukharev (2005), Interannual variations of total ozone at northern midlatitudes correlated with stratospheric EP flux and potential vorticity, *J. Atmos. Sci.*, *62*, 3724–3740.

Huang, T. Y. W., and G. P. Brasseur (1993), Effect of long-term solar variability in a two-dimensional interactive model of the middle atmosphere, *J. Geophys. Res.*, *98*, 20,413–20,427.

Huesmann, A. S., and M. H. Hitchman (2001), The stratospheric quasi-biennial oscillation in the NCEP reanalyses: Climatological structures, *J. Geophys. Res.*, *106*, 11,859–11,874.

Jackman, C. H., and R. D. McPeters (1985), The response of ozone to solar proton events during Solar Cycle 21: A theoretical interpretation, *J. Geophys. Res.*, *90*, 7955–7966.

Jackman, C. H., A. R. Douglass, R. B. Rood, R. D. McPeters, and P. E. Meade (1990), Effect of solar proton events on the middle atmosphere during the past two solar cycles as computed using a two-dimensional model, *J. Geophys. Res.*, *95*, 7417–7428.

Jackman, C. H., A. R. Douglass, S. Chandra, R. S. Stolarski, J. E. Rosenfield, J. A. Kaye, and E. R. Nash (1991), Impact of interannual variability (1979–1986) of transport and temperature on ozone as computed using a two-dimensional photochemical model, *J. Geophys. Res.*, *96*, 5073–5079.

Jackman, C. H., E. L. Fleming, S. Chandra, D. B. Considine, and J. E. Rosenfield (1996), Past, present, and future modeled ozone trends with comparisons to observed trends, *J. Geophys. Res.*, *101*, 28,753–28,767.

Jackman, C. H., M. T. DeLand, G. J. Labow, E. L. Fleming, D. K. Weisenstein, M. K. W. Ko, M. Sinnhuber, and J. M. Russell (2005), Neutral atmospheric influences of the solar proton events in October–November 2003, *J. Geophys. Res.*, *110*, A09S27, doi:10.1029/2004JA010888.

Jiang, X., C. D. Camp, R. Shia, D. Noone, C. Walker, and Y. L. Yung (2004), Quasi-biennial oscillation and quasi-biennial oscillation-annual beat in the tropical total column ozone: A two-dimensional model simulation, *J. Geophys. Res.*, *109*, D16305, doi:10.1029/2003JD004377.

Jones, D. B. A., H. R. Schneider, and M. B. McElroy (1998), Effects of the quasi-biennial oscillation on the zonally averaged transport of tracers, *J. Geophys. Res.*, *103*, 11,235–11,249.

Kalnay, E., et al. (1996), The NCEP/NCAR 40-year reanalysis project, *Bull. Am. Meteor. Soc.*, *77*, 437–471.

Kanamitsu, M., W. Ebisuzaki, J. Woollen, S.-K. Yang, J. J. Hnilo, M. Fiorino, and G. L. Potter (2002), NCEP-DOE AMIP-II reanalysis (R-2), *Bull. Am. Meteor. Soc.*, *83*, 1631–1643.

Kinnersley, J. S., and K. K. Tung (1998), Modeling the global interannual variability of ozone due to the equatorial QBO and to extratropical planetary wave activity, *J. Atmos. Sci.*, *55*, 1417–1428.

Kinnersley, J. S., and K. K. Tung (1999), Mechanisms for the extratropical QBO in circulation and ozone, *J. Atmos. Sci.*, *56*, 1942–1962.

Kinnison, D. E., K. E. Grant, P. S. Connell, D. A. Rotman, and D. J. Wuebbles (1994), The chemical and radiative effects of the Mount Pinatubo eruption, *J. Geophys. Res.*, *99*, 25,705–25,731.

Kirchner, I., G. L. Stenchikov, H.-F. Graf, A. Robock, and J. C. Antuna (1999), Climate model simulation of winter warming and summer cooling following the 1991 Mount Pinatubo volcanic eruption, *J. Geophys. Res.*, *104*, 19,039–19,055.

Kistler, R., et al. (2001), The NCEP-NCAR 50-year reanalysis: Monthly means CD-ROM and documentation, *Bull. Am. Meteor. Soc.*, *82*, 247–267.

Ko, M. K. W., N. D. Sze, M. Livshits, M. B. McElroy, and J. A. Pyle (1984), The seasonal and latitudinal behavior of trace gases and O_3 as simulated by a two-dimensional model of the atmosphere, *J. Atmos. Sci.*, *41*, 2381–2408.

Kodera, K., and Y. Kuroda (2002), Dynamical response to the solar cycle, *J. Geophys. Res.*, *107*(D24), 4749, doi:10.1029/2002JD002224.

Lee, H., and A. K. Smith (2003), Simulation of the combined effects of solar cycle, quasi-biennial oscillation, and volcanic forcing on stratospheric ozone changes in recent decades, *J. Geophys. Res.*, *108*(D2), 4049, doi:10.1029/2001JD001503.

Liley, J. B., P. V. Johnston, R. L. McKenzie, A. J. Thomas, and I. S. Boyd (2000), Stratospheric NO_2 variations from a long time series at Lauder, New Zealand, *J. Geophys. Res.*, *105*, 11,633–11,640.

Lindzen, R. S. (1981), Turbulence and stress owing to gravity wave and tidal breakdown, *J. Geophys. Res.*, *86*, 9707–9714.

McPeters, R. D., G. J. Labow, and J. A. Logan (2007), Ozone climatological profiles for satellite retrieval algorithms, *J. Geophys. Res.*, *112*, D05308, doi:10.1029/2005JD006823.

Minschwaner, K., and D. E. Siskind (1993), A new calculation of nitric oxide photolysis in the stratosphere, mesosphere, and lower thermosphere, *J. Geophys. Res.*, *98*, 20,401–20,412.

Mote, P. W., et al. (1996), An atmospheric tape recorder: The imprint of tropical tropopause temperatures on stratospheric water vapor, *J. Geophys. Res.*, *101*, 3989–4006.

Mote, P. W., T. J. Dunkerton, M. E. McIntyre, E. A. Ray, P. H. Haynes, and J. M. Russell III (1998), Vertical velocity, vertical diffusion, and dilution by midlatitude air in the tropical lower stratosphere, *J. Geophys. Res.*, *103*, 8651–8666.

Newman, P. A., M. R. Schoeberl, R. A. Plumb, and J. E. Rosenfield (1988), Mixing rates calculated from potential vorticity, *J. Geophys. Res.*, *93*, 5221–5240.

Newman, P. A., E. R. Nash, and J. E. Rosenfield (2001), What controls the temperature of the Arctic stratosphere during the spring?, *J. Geophys. Res.*, *106*, 19,999–20,010.

Oort, A. H. (1983), *Global Atmospheric Circulation Statistics, 1958–1983*, NOAA professional paper 14.

Orsolini, Y. J., and V. Limpasuvan (2001), The North Atlantic oscillation and the occurrences of ozone miniholes, *Geophys. Res. Lett.*, *28*, 4099–4102.

Park, J. H., M. K. W. Ko, C. H. Jackman, R. A. Plumb, J. A. Kaye, and K. H. Sage (Eds.) (1999), Models and measurements intercomparison II, in *NASA Tech. Memo.*, *TM-1999-209554*.

Plumb, R. A., and J. D. Mahlman (1987), The zonally averaged transport characteristics of the GFDL general circulation/transport model, *J. Atmos. Sci.*, *44*, 298–327.

Randel, W. J. (1987), The evaluation of winds from geopotential height data in the stratosphere, *J. Atmos. Sci.*, *44*, 3097–3120.
Randel, W. J., and R. R. Garcia (1994), Application of a planetary wave breaking parameterization to stratospheric circulation statistics, *J. Atmos. Sci.*, *51*, 1157–1168.
Randel, W. J., and F. Wu (1996), Isolation of the ozone QBO in SAGE II data by singular-value decomposition, *J. Atmos. Sci.*, *53*, 2546–2559.
Randel, W. J., F. Wu, R. Swinbank, J. Nash, and A. O'Neill (1999), Global QBO circulation derived from UKMO stratospheric analyses, *J. Atmos. Sci.*, *56*, 457–474.
Randel, W. J., F. Wu, A. Gettelman, J. M. Russell III, J. M. Zawodny, and S. J. Oltmans (2001), Seasonal variation of water vapor in the lower stratosphere observed in Halogen Occultation Experiment data, *J. Geophys. Res.*, *106*, 14,313–14,325.
Randel, W. J., F. Wu, and R. Stolarski (2002), Changes in column ozone correlated with the stratospheric EP flux, *J. Meteorol. Soc. Jpn.*, *80*, 849–862.
Ray, E. A., F. L. Moore, J. W. Elkins, G. S. Dutton, D. W. Fahey, H. Vomel, S. J. Oltmans, and K. H. Rosenlof (1999), Transport into the Northern Hemisphere lowermost stratosphere revealed by in situ tracer measurements, *J. Geophys. Res.*, *104*, 26,565–26,580.
Reid, S. J., A. F. Tuck, and G. Kildaris (2000), On the changing abundance of ozone minima at Northern midlatitudes, *J. Geophys. Res.*, *105*, 12,169–12,180.
Rosenfield, J. E., P. A. Newman, and M. R. Schoeberl (1994), Computations of diabatic descent in the stratospheric polar vortex, *J. Geophys. Res.*, *99*, 16,677–16,689.
Rosenfield, J. E., D. B. Considine, P. E. Meade, J. T. Bacmeister, C. H. Jackman, and M. R. Schoeberl (1997), Stratospheric effects of Mount Pinatubo aerosol studied with a coupled two-dimensional model, *J. Geophys. Res.*, *102*, 3649–3670.
Rossow, W. B., and E. N. Duenas (2004), The international satellite cloud climatology project (ISCCP) web site, *Bull. Am. Meteor. Soc.*, *85*, 167–172.
Salby, M. L., and P. Callaghan (2004a), Evidence of the solar cycle in the general circulation of the stratosphere, *J. Clim.*, *17*, 34–46.
Salby, M. L., and P. Callaghan (2004b), Systematic changes of Northern Hemisphere ozone and their relationship to random interannual changes, *J. Clim.*, *17*, 4512–4521.
Sander, S. P., et al. (2003), Chemical kinetics and photochemical data for use in atmospheric studies, evaluation number 14, JPL Publ., 02-25.
Schneider, H. R., M. K. W. Ko, N. D. Sze, G.-Y. Shi, and W.-C. Wang (1989), An evaluation of the role of eddy diffusion in stratospheric interactive two-dimensional models, *J. Atmos. Sci.*, *46*, 2079–2093.
Smyshlyaev, S. P., V. L. Dvortsov, M. A. Geller, and V. A. Yudin (1998), A two-dimensional model with input parameters from a general circulation model: Ozone sensitivity to different formulations for the longitudinal temperature variation, *J. Geophys. Res.*, *103*, 28,373–28,387.
Solomon, S., R. W. Portmann, R. R. Garcia, L. W. Thomason, L. R. Poole, and M. P. McCormick (1996), The role of aerosol variations in anthropogenic ozone depletion at northern midlatitudes, *J. Geophys. Res.*, *101*, 6713–6727.
Solomon, S., et al. (1998), Ozone depletion at midlatitudes: Coupling of volcanic aerosols and temperature variability to anthropogenic chlorine, *Geophys. Res. Lett.*, *25*, 1871–1874.
Steinbrecht, W., H. Claude, U. Kohler, and K. P. Hoinka (1998), Correlations between tropopause height and total ozone: Implications for long-term changes, *J. Geophys. Res.*, *103*, 19,183–19,192.
Steinbrecht, W., H. Claude, U. Kohler, and P. Winkler (2001), Interannual changes of total ozone and Northern Hemisphere circulation pattern, *Geophys. Res. Lett.*, *28*, 1191–1194.
Stolarski, R. S., P. Bloomfield, R. D. McPeters, and J. R. Herman (1991), Total ozone trends deduced from Nimbus-7 TOMS data, *Geophys. Res. Lett.*, *18*, 1015–1018.
Stolarski, R. S., A. R. Douglass, S. Steenrod, and S. Pawson (2006), Trends in stratospheric ozone: Lessons learned from a 3D chemical transport model, *J. Atmos. Sci.*, *63*, 1028–1041.
Tie, X., G. P. Brasseur, B. Briegleb, and C. Granier (1994), Two-dimensional simulation of Pinatubo aerosol and its effect on stratospheric ozone, *J. Geophys. Res.*, *99*, 20,545–20,562.
Uppala, S. M., et al. (2005), The ERA-40 re-analysis, *Q. J. R. Meteorol. Soc.*, *131*, 2961–3012.
Wallace, J. M., R. L. Panetta, and J. Estberg (1993), Representation of the equatorial stratospheric quasi-biennial oscillation in EOF phase space, *J. Atmos. Sci.*, *50*, 1751–1762.
Weisenstein, D. K., M. K. W. Ko, J. M. Rodriguez, and N. D. Sze (1991), Impact of heterogeneous chemistry on model-calculated ozone change due to High Speed Civil Transport aircraft, *Geophys. Res. Lett.*, *18*, 1991–1994.
Weisenstein, D., M. K. W. Ko, I. Dyominov, G. Pitari, L. Ricciardulli, G. Visconti, and S. Bekki (1998), A model intercomparison of the effects of sulfur emissions from HSCT aircraft, *J. Geophys. Res.*, *103*, 1527–1546.
Weisenstein, D. K., et al. (2004), Separating chemistry and transport effects in 2-D models, *J. Geophys. Res.*, *109*, D18310, doi:10.1029/2004JD004744.
World Meteorological Organization (WMO) (1999), Scientific assessment of ozone depletion: 1998, Rep. 44, Global Ozone Research and Monitoring Project, Geneva.
World Meteorological Organization (WMO) (2003), Scientific assessment of ozone depletion: 2002, Rep. 47, Global Ozone Research and Monitoring Project, Geneva.
World Meteorological Organization (WMO) (2007), Scientific assessment of ozone depletion: 2006, Rep. 50, Global Ozone Research and Monitoring Project, Geneva.
Wu, D. L., et al. (2003), Mesospheric temperature from UARS MLS: retrieval and validation, *J. Atmos. Sol.-Terr. Phys.*, *65*, 245–267.
Ziemke, J. R., S. Chandra, R. D. McPeters, and P. A. Newman (1997), Dynamical proxies of column ozone with applications to global trend models, *J. Geophys. Res.*, *102*, 6117–6129.

E. L. Fleming and C. H. Jackman, NASA Goddard Space Flight Center, Code 613.3, Greenbelt Road, Greenbelt, MD 20771-0001, USA. (fleming@kahuna.gsfc.nasa.gov; charles.h.jackman@nasa.gov)
M. K. W. Ko, NASA Langley Research Center, Mail Stop 401B, Hampton, VA 23681, USA. (malcolm.k.ko@nasa.gov)
D. K. Weisenstein, Atmospheric and Environmental Research, Inc., 131 Hartwell Avenue, Lexington, MA 02421, USA. (weisenstein@aer.com)